Experiments in Fluids (2024) 65:117
https://doi.org/10.1007/s00348-024-03846-5

RESEARCH ARTICLE

# Growth of organized flow coherent motions within a single-stream shear layer: 4D-PTV measurements

**Ankit K. Gautam[1] · Daniel Livescu[2] · Ricardo Mejia-Alvarez[1]**

Received: 6 July 2023 / Revised: 15 March 2024 / Accepted: 24 June 2024


**Abstract**

This study investigates the evolution of a single-stream shear layer (SSSL) originating from a wall boundary layer past a backward-facing step. Utilizing a time-resolved 3D-Particle Tracking Velocimetry (4D-PTV) technique, we track the trajectories of fluorescent particles to gain insight into the flow characteristics of the SSSL. A compact water tunnel facility ($Re_\tau = 1\,240$) is fabricated to obtain an SSSL with a perpendicular slow entrainment stream past the separation edge. A hybrid interpolation approach that combines ensemble binning and Gaussian weighting is implemented to derive minimally filtered mean and instantaneous lower- and higher-order flow field parameters. Spanwise-dominant coherent motion accompanied by finer flow scales is observed to grow due to flow entrainment through "nibbling" actions of small-scale vortices, "engulfing" by large-scale vortices, and vortex pairing events. Furthermore, the non-zero-speed stream edge grows relatively faster than the zero-speed stream edge, showing a strong asymmetry in mixing composition across a mixing layer. The SSSL reaches self-similarity at a streamwise distance of $\approx 55\,\theta_0$, where $\theta_0$ is the initial momentum thickness from the separation edge, i.e., considerably shorter than reported in previous studies. A literature comparison of growth rate parameters raises intriguing questions regarding a potential inclusive growth scaling unifying the free shear layers. A turbulent kinetic energy (TKE) budget analysis reveals a negative production region immediately downstream of the separation edge attributed to a large positive streamwise gradient of streamwise velocity. In the self-similar region, the phase-averaged flow mapping demonstrates a larger concentration of turbulence production rate around the outer edges of spanwise vortices, specifically at the intersection of braids and vortices. Furthermore, a spatial separation exists in the regions of peak production and dissipation rates within the vortex core region favoring dissipation. The braids exhibit a larger concentration of turbulence diffusion rates, indicating their function as a conduit for exchanging turbulence between neighboring coherent motions.

## 1 Introduction

Two-stream shear layers (TSSL), formed by an unbounded mixing interaction between two streams, is a canonical turbulent flow configuration. In comparison, a single-stream shear layer (SSSL) is formed when one of the streams has zero initial streamwise velocity. The ubiquity of the shear mixing layers in diverse areas of natural flows and engineering industries makes them widely studied, with various configurations related to specific practical applications. Geological flows include rivers and estuaries (Harang et al 2014) and hot plumes within the Earth's mantle layer (Campbell and Turner 1985), to mention a couple. Practical engineering applications include inertial confinement fusion (Weber et al 2014), combustion mixing in aircraft jet engines (Talbot et al 2013), or internal combustion engines, among others.

SSSL and TSSL have received significant attention in the past 70 years. The scientific community has been dramatically influenced by the visuals of the flow coherent motions within a planar TSSL, reported in the seminal work of Brown and Roshko (1974). Since then, a plethora of research work concerning the flow structure organization and physical characteristics of the mixing layers at different velocity and density ratios are reported (Hussain and Zaman 1985;

✉ Ricardo Mejia-Alvarez
rimejal@msu.edu

Ankit K. Gautam
gautama1@msu.edu

Daniel Livescu
livescu@lanl.gov

[1] Department of Mechanical Engineering, Michigan State University, 1449 Engineering Research Ct., East Lansing, MI 48823, US

[2] CCS-2 Computational Physics, Los Alamos National Laboratory, Los Alamos, NM 87544, US

Published online: 23 July 2024

Lasheras et al 1986; Dimotakis 1991; D'Ovidio and Coats 2013). Keller et al (1988) studied the unsteady behavior and organization within the SSSL under forced vibrations, and Kailas and Narasimha (1999) implemented wavelet transform to isolate the levels of organization in the layer. Numerical and computational studies (DNS and LES) (Rogers and Moser 1994; Balaras et al 2001; McMullan et al 2015; McMullan and Garrett 2016; Suryanarayanan and Narasimha 2017; Sharan et al 2019; Baltzer and Livescu 2020) have gathered considerable success in resolving the flow coherent motions of a mixing layer at increasingly higher spatial and temporal resolution.

The quantitative studies have revealed the complex nature of a mixing layer (Wygnanski and Fiedler 1970; Patel 1973; Mehta and Westphal 1986; Bell and Mehta 1990). While the studies agree on a universal self-similar behavior of mixing layers, the normalized distance necessary to attain those conditions shows wide disagreement (Bell and Mehta 1990; Morris and Foss 2003). Additionally, simple physical parameters, such as the growth rates of the mixing layer width or momentum thickness, do not show consistent values throughout different studies (Brown and Roshko 1974; Browand and Latigo 1979; Browand and Troutt 1985; Mehta and Westphal 1986). This led to the consensus that the initial flow condition of a mixing layer might be one of the controlling parameters for its transition toward universal behavior (Dimotakis 1991).

Despite the similar qualitative behavior of SSSL and TSSL, the two do not agree on flow characteristics such as the growth rates of shear layer width. For example, scaling considered appropriate for momentum and vorticity thickness (Brown and Roshko 1974; Browand and Troutt 1985) is only reasonably "universal" for TSSL but falls short for SSSL. Seeking universal growth rate patterns, Suryanarayanan and Narasimha (2017) conducted numerical investigations and comparisons with past studies. They maintain that apart from initial conditions, downstream conditions notably influence the growth rate of a single-stream shear layer.

On the other hand, SSSL studies available in the literature lack high spatial resolution measurements; and to the best of our knowledge, three-dimensional time-resolved high-resolution measurements for an SSSL do not exist either. Thus, it is possible to further our understanding of SSSLs using the current advancements in laser-based diagnostics capabilities.

In the present study, we use a time-resolved 3D Particle Tracking Velocimetry (4D-PTV) to investigate the transition of the wall boundary layer into an SSSL and its further development into a self-similar SSSL. The flow apparatus adopted in the present study is similar to Hussain and Zaman (1985); Morris and Foss (2003) with a backward-facing separation step with a slow perpendicular entrainment stream. The results discussed in the current article encompass the 3D visualization of coherent and organizational flow features and their statistical attributes within distinct regions of the mixing layer.

The rest of the discussion is organized as follows: The design and working principles of the water tunnel facility and flow diagnostics used for the current experiments are initially discussed, followed by an outline of the method used to interpolate unstructured data onto a structured grid. Next, we discuss the characteristics of the wall boundary layer captured upstream of the backward-facing step, followed by a detailed discussion of three distinct regions of the SSSL: viscous-dominated, transitional, and self-similar region. In addition, we outline the mixing layer's low- and higher-order statistical properties, including a turbulent kinetic energy budget analysis for the above-mentioned flow regions of the SSSL. We conclude our discussion with phase-averaged flow maps of relevant turbulent quantities and their organization within the flow coherent motions.

## 2 Experimental setup

### 2.1 Water tunnel facility

Figure 1 shows a schematic of the closed-loop, compact, high Reynolds number water tunnel facility fabricated for this study. The facility has five major sections: the plenum, contraction duct, test section, triangular header, and recirculation tank. The test section is fabricated with acrylic for optical access.

The test section is a downscale (1:10) model of the wind tunnel test section used by Morris and Foss (2003). The primary inlet delivers a water flow with a free-stream velocity of $U_\infty \approx 1.37$ m/s as it develops over the 600 mm long developing section of spanwise width 150 mm and half-height $h_c = 50$ mm. The bottom wall boundary layer separates at the 90° separation edge. The developing section is long enough to ensure that the bottom-wall boundary layer becomes turbulent. This developing section is also short enough to prevent the top- and bottom-wall boundary layers from interacting with each other prior to the backstep separation point. The secondary inlet of the test section accepts a relatively low-velocity stream over a streamwise length of 975 mm with a nominal speed of $\sim 0.035U_\infty$ in the vertical direction, perpendicular to the primary flow. The peculiar velocity value for the slower stream comes from the estimated entrainment velocity for the slower stream (Brown and Roshko 1974; Morris and Foss 2003), thus replenishing the entrained fluid (or mass flux) in the vertical direction.

Before entering the test section, the high-speed primary flow passes through a contraction duct (Fig. 1). The duct attenuates the wall-normal and spanwise fluctuations, and the boundary layer thickness, without flow separation. A

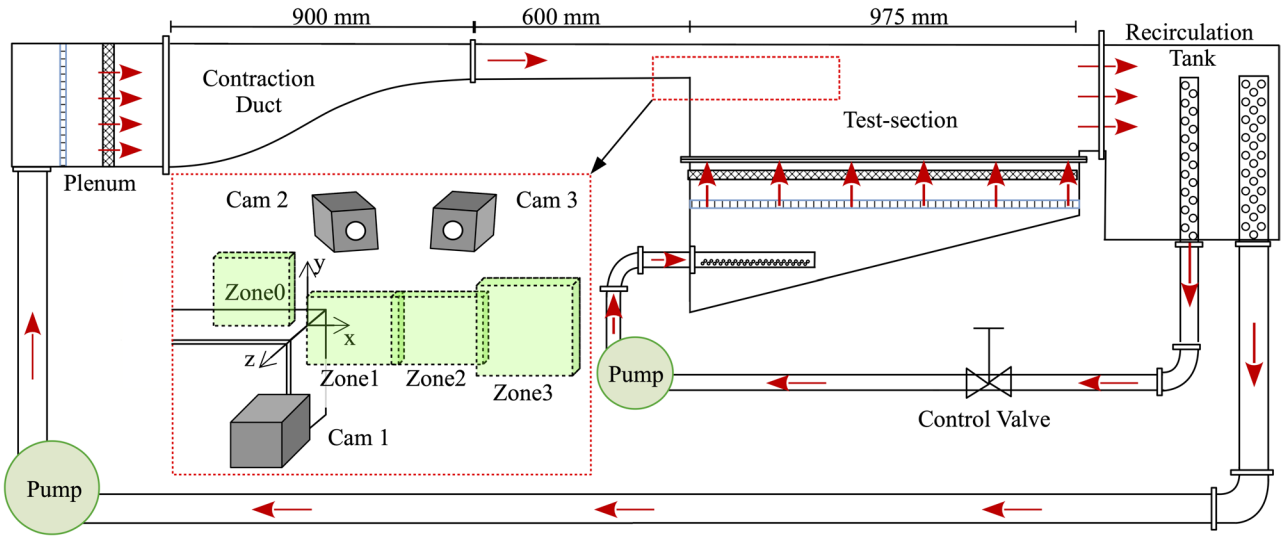


**Fig. 1** Schematic of the water tunnel facility. *Inset* shows the arrangement of cameras pointing over the region of interest demarcated by Zone0 ($-23 \lesssim x/\theta_0 \lesssim -7$), Zone1 ($0 \lesssim x/\theta_0 \lesssim 22$), Zone2 ($22 \lesssim x/\theta_0 \lesssim 43$) to Zone3 ($42 \lesssim x/\theta_0 \lesssim 73$), $\theta_0$ is initial momentum thickness estimated at upstream location, $x/\theta_0 \approx -7.35$ from the separation edge. Note the two distinct flow circuits with dedicated centrifugal pumps

fifth-order polynomial curve and contraction ratio of 6:1 is adopted to design the duct's walls (Wetzel and Arndt 1994). A more aggressive contracting profile at the bottom compared with the lateral sides ensures a larger suppression factor for the bottom wall boundary layer, while the top panel of the duct is kept flat as the current study focuses on the bottom-wall boundary layer first developing and then separating at the edge of the backward-facing step. A contraction duct is unnecessary for the upward-moving stream (secondary inlet in the test section) on account of flow being laminar; nonetheless, a honeycomb and flow-conditioning meshes are employed to ensure flow uniformity.

Both plenum and triangular header are installed with a perforated plate (hole diameter 12.5 mm) and a honeycomb (hole diameter 3 mm, thickness 30 mm). The perforated plate, honeycomb, and screen break down larger eddies, homogenize the velocity distribution, and reduce flow fluctuations in cross-stream and spanwise directions. A settling zone follows the screen to allow grid turbulence (if produced) to decay. In addition, to maintain a flatter flow profile across the secondary flow cross-section, an inclined triangular header, inspired by the study of London et al (1968), is designed and fabricated.

The flow rate of the high-speed stream is controlled with a variable frequency drive (VFD) (Mitsubishi E700 series) that modifies the angular speed of the motor (WEG Industries) that drives the centrifugal pump (SHURflo, LLC). The flow rate of the low-speed stream is controlled using a gate valve. The working fluid for these experiments is tap water at 20°C and local atmospheric pressure (101.7 kPa average).

## 2.2 Flow imaging system

The velocity field is captured in this study with time-resolved laser-based diagnostics. The flow is illuminated with a high-speed dual-head Nd:YLF laser (DM30-527DH, Photonics Inc., USA) with wavelength 527 nm, maximum repetition 10 kHz (each head), and maximum energy per pulse 70 mJ. The laser beam is reshaped into a 6-mm-thick slab of width $\approx$ 49 mm at the test section with a set of laser-grade cylindrical and spherical lenses. The height of the region of interest (ROI) is $\approx$ 35 mm and is defined by the aspect ratio of the CMOS sensor (width/height = 8/5). Three high-speed cameras, arranged as shown in Fig. 1, captured images of fluorescent particles suspended in the flow. The cameras (Phantom v2512) use CMOS arrays of size 1280 px $\times$ 800 px and can capture at frame rates of 25 700 frames per second at full resolution. The camera lenses are set with an f-stop of *f*/11 to ensure an appropriate depth of field across the illuminated volume. The lenses are mounted to the cameras with Scheimpflug mounts to correct for angular distortions. Time-resolved measurements are obtained each time at repetition rates of 4 kHz. The imaging system is calibrated with a two-level double-sided 3D calibration plate (058-5, LaVision, Germany). This plate is composed by a dotted grid with grid spacing 5 mm, dot diameter 1.2 mm, and level separation 1 mm. The plate is set parallel to the

streamwise–cross-stream plane ($x - y$ plane in Fig. 1). This initial spatial calibration is refined with volume self-calibration (Wieneke 2008) (implemented with LaVision—DaVis), in which 3D disparity maps of particles imaged simultaneously with the three cameras are generated in local sub-volumes and used to correct the calibration function obtained with the physical target. After self-calibration, the triangulation error for particle location is reduced to sub-pixel values (≈0.018 px) (Schanz et al 2016).

The flow is captured over four zones, Zone0–Zone3, as indicated in Fig. 1. Zone0 is situated within the tunnel, upstream of the backward-facing step, while Zone1–Zone3 capture the development of the SSSL. Based on the volume calibration, average spatial resolution in the current experiments is estimated to be ≈ 24 px/mm for Zone0–Zone2 and ≈ 17 px/mm for Zone3. The flow is seeded with fluorescent particles fabricated in-house following Pedocchi et al (2008), with average density ≈ 1.2 g/cm$^3$ and size distribution with average diameter 21.5 $\mu$m and standard deviation 6.5 $\mu$m. The average particle image density within the captured zones ranges between 0.05 and 0.07 particles per pixel. A comparatively sparser particle number density is noticed in the high-strain region of the mixing layer (Zone1–Zone3) and the near-wall region of the boundary layer (Zone0). As the SSSL grows, the cameras need to zoom out to capture the whole extent of the shear layer, slightly decreasing the spatial resolution for Zone3. The average inter-particle distance, $d_{\mathrm{p-p}}$ obtained over the 3D-PTV fields within Zone0–Zone2 and Zone3, is estimated to be ≈0.9 mm and ≈ 1.08 mm, respectively.

### 2.3 4D-PTV Technique: shake-the-box

This study uses the Shake-The-Box (STB) algorithm (Wieneke 2012; Schanz et al 2016) implemented in LaVision—DaVis, to reduce time-resolved three-dimensional velocity fields. This algorithm can provide accurate velocity measurements at high particle density images. An essential advantage of STB over 2D- and 3D-PIV algorithms is that flow information is obtained in the Lagrangian frame of reference by tracking individual particles, eliminating spatial filtering introduced by the interrogation windows or voxels typically used in 2D- and 3D-PIV. In addition, STB implements a spurious-particle detection scheme that uses spatial and temporal information around a particle to remove tracks that do not fit the surrounding particle trajectories, resulting in virtually no ghost particles (< 0.04%) (Schanz et al 2016).

As particle motion detection advances in STB, a second-order polynomial is fitted through the particle trajectories over every five time steps until the particle is "lost" by the algorithm or it exits the ROI (Wiener 1949). The fitted polynomials are used to predict the position of particles in the next time step. Subsequently, final 3D position of particles is obtained by iterative process of adjusting or "shaking" the position of reconstructed particles with the aim to minimize the local residual intensity between the back-projected particle image intensity fields and the originally captured image fields from all cameras. Thereafter, velocity and material derivative at each particle position are obtained. Consequently, these flow details are obtained in the Lagrangian frame of reference in an evolving unstructured grid formed by connecting measurement points (particles) varying with every instantaneous reconstructed particle field. For a more complete flow description, the Lagrangian information is then interpolated onto a structured grid to develop an Eulerian flow description.

Among several interpolation methods, Gesemann (2015) fit B-splines through particle tracks followed by an optimization process that employs governing flow equations to minimize the error between measured and interpolated data. Casa and Krueger (2013) employed radial basis functions (RBFs) to regularize scattered data onto a structured grid which they found to be computationally more demanding than the Gaussian weighting (GW) interpolation technique (Agüí and Jimenez 1987. In addition, the gain in accuracy achieved with RBFs was relatively smaller, making the GW interpolation technique a more efficient choice. A more advanced form of the data interpolation or assimilation technique is Vortex-In-Cell plus (VIC+) (Schneiders and Scarano 2016) and its fine-scale reconstruction version VIC# (Jeon et al 2022). These methods employ governing flow equations and divergence constraints to interpolate and minimize errors. In the present study, adaptive ensemble binning (Raiola et al 2020) is implemented to get the mean velocity field. On the other hand, instantaneous velocity and higher-order parameters (such as Reynolds stress tensor and TKE budget terms) fields are derived by adopting a computationally inexpensive approach that combines the technique suggested by Tirelli et al (2023) and adaptive Gaussian weighting (AGW) (Agüí and Jimenez 1987) to interpolate the PTV data onto a structured grid. These methods are discussed in detail in the next section.

## 3 Data analysis

### 3.1 Adaptive ensemble binning

3D-PTV captures relatively sparser particle distributions resulting in larger inter-particle distances and lower instantaneous spatial resolution. As discussed in the previous section, to achieve a high-resolution instantaneous velocity field over a structured grid, advanced data assimilation and reconstruction techniques are more effective. However, to derive high-resolution mean fields, ensemble binning (EB) of instantaneous PTV particle data into structured bins

is favored (Raiola et al 2020), provided enough particles within each bin are collected to ensure statistical convergence. Given the total number of available instantaneous PTV fields ($N_{snap}$), reconstructed particle number density ($N_{ppp}$, in particle per pixel) ranging between 0.015 and 0.02 across captured zones, and the average number of particles ($N_p$) per bin for a spherical averaging bin of diameter, $b$ (in voxels) are related by

$$N_p^{min} = \frac{4}{3}\pi\left(\frac{b}{2}\right)^3 \frac{N_{ppp}\,N_{snap}}{L_z} \quad (1)$$

where $L_z$ is the spanwise depth of captured 3D-region in voxels (Agüera et al 2016). This formula guides the selection of the bin size based on other available parameters. In this study, Zone0–Zone2 and Zone3 adopt a grid spacing (bin size) of 0.3 mm and 0.45 mm, respectively, equating to approximately 8 voxels in size. For the adaptive ensemble binning discussed in this section, a 50% overlap between adjacent spherical bins is utilized, resulting in a spherical bin diameter of $b = 12$ voxels, ensuring statistical convergence and smoother mean fields at the grid point centered at the bin. Table 1 lists the average number of particles per bin, $N_p$, obtained for each respective zone over the total number of realizations. Notably, $N_p$ across all zones nearly equals or exceeds the average minimum number of particles per bin, $N_p^{min}$, necessary for convergence according to equation 1.

Simple particle data binning assumes a top-hat function weighting for an ensemble of particles within the bin, resulting in increased spatial filtering, particularly in areas with significant spatial gradients. Thus, a locally adaptive Gaussian weighting function, represented as an ellipsoid with aspect ratios determined through local singular value decomposition, is employed to derive the mean velocity fields, mirroring the approach outlined by Novara et al (2012). As an aside, refer Raiola et al (2020) for a more detailed account of determining the aspect ratio for the anisotropic Gaussian weighting function using Hessian for each velocity component. Higher-order statistics, i.e., stress tensor components are derived using the mean velocity field, obtained via adaptive ensemble binning, employing equal weight for particles within the bin (top-hat filter). This is primarily for comparison with the mean stress fields derived from an inexpensive interpolation method, detailed in the subsequent section. On a separate note, the polynomial fitting method proposed by Agüera et al (2016) to obtain mean velocity and stress tensor fields is also assessed which showed negligible variance compared to the adaptive ensemble binning approach.

On the other hand, instantaneous flow fields are obtained by adapting a simple yet ingenious technique outlined by Tirelli et al (2023). In this technique, the mean velocity components obtained using the adaptive ensemble binning method are interpolated using a spline function at PTV particle locations within each instantaneous 3D-PTV field. The interpolated mean velocity is then subtracted from the measured value, facilitating the determination of instantaneous velocity fluctuations at the individual particle locations. Subsequently, the PTV fluctuation field is mapped onto a structured Eulerian grid that results in an instantaneous velocity fluctuation map with reduced systematic errors compared to the mapping using the original PTV velocity data prior to mean subtraction (Tirelli et al 2023). We discussed the flow field interpolation technique, i.e., adaptive Gaussian weighting (AGW) used for mapping on Eulerian grids is discussed in the following section.

Furthermore, alongside velocity fluctuation components, double and triple correlation terms at each particle position are also obtained, consequently, deriving instantaneous maps for Reynolds stress components and terms in the turbulent kinetic energy (TKE) budget. This approach offers a significant advantage over solely deriving these terms from instantaneous velocity fluctuation maps, thereby circumventing spatial filtering effects—an important finding of the present work further discussed in the next section. The instantaneous maps of dissipation rate, however, are obtained using the instantaneous velocity fluctuation maps as the local computation at PTV points of dissipation rate is not viable. It can be computed over an instantaneous unstructured grid, but this aspect lies beyond the scope of the present work.

**Table 1** Minimum number of particles per bin, $N_p^{min}$ necessary for convergence as per equation 1 for a given total instantaneous realizations $N_{snap}$ and spherical bin size $b = 12$ voxels. $N_p$ is the approximate average number of particles per bin obtained across different zones

| | $N_{snap}$ | $N_p^{min}$ | $N_p$ |
|---|---|---|---|
| Zone0 | 8000 | 950 | 1200 |
| Zone1 | 4000 | 400 | 500 |
| Zone2 | 16,000 | 1,650 | 1600 |
| Zone3 | 48,000 | 7,200 | 9500 |

## 3.2 Adaptive Gaussian weighting

Gaussian weighting is a mesh-less data interpolation method introduced by Agüí and Jimenez (1987). The method uses a Gaussian function to assign weight, $w_i$ to the Lagrangian data points given by:

$$w_i = \exp\left[-\frac{||x_h - x_i||^2}{2H^2}\right] \tag{2}$$

where $x_h$ and $x_i$ are the locations of Eulerian grid points and scattered Lagrangian points around the grid point location, respectively. The numerator within the parenthesis is the L2 norm or the Euclidean distance between $x_h$ and $x_i$, and the denominator quantity, $H$, is the Gaussian function's rms width. The flow quantity, $\phi_h$ at a grid point such as velocity fluctuations and double- or triple-order correlation terms, is interpolated using:

$$\phi_h = \frac{\sum_i^{n_p} w_i \phi_i}{\sum_i^{n_p} w_i} \tag{3}$$

where $\phi_i$ is the locally derived flow quantity at Lagrangian points. The Gaussian function rms width, $H$, determines the degree of overlap between functions employed at adjacent grid nodes, consequently determining the smoothness of the interpolated field. A higher overlap will over-smooth the field, while a smaller overlap can lead to holes and unnatural fluctuations within the flow field. Agüí and Jimenez (1987) found $H = 0.877h$ to be an appropriate value, where $h$ is grid spacing. In a similar interpolation approach (Schneiders and Scarano 2016), based on the tracked particle density and flow resolving capability of the data assimilation algorithm (VIC+), the width of the Gaussian radial basis function is chosen to be $1.1h$. The appropriate value for width depends on data density and reasonable validity of the interpolated data.

Despite an effort to ensure a homogeneous suspension of tracer particles, anisotropic stress in the flow results in regions of sparse particle number densities. Thus, a minimum $n_p$ number of scattered Lagrangian points nearest to a grid point are chosen to implement adaptive Gaussian weighting (AGW), rendering it adaptive to sparser regions of the flow. Notably, different levels of overlap or varied Gaussian function rms widths, $H$, along with varying particle counts, $n_p$ around each grid point for interpolation, are investigated to assess their effect on higher-order flow quantities. The influence of interpolation parameters on the instantaneous flow field is anticipated, and while an effect is observed, it is not particularly pronounced. The optimal compromise is achieved by selecting a Gaussian rms width of $H = 1.24h$ and considering $n_p = 10$ number of nearest particles around each grid point that resulted in smoother flow profiles. On the other hand, the mean fields derived out of all instantaneous fields for respective lower- and higher-order parameters obtained using AGW indicate that changing the width or the nearest number of particles has minimal impact on the mean higher-order quantities. Refer Appendix A.1 and A.2 for more details on effect of interpolation parameters and tests regarding data convergence, respectively.

On a separate note, a mean field obtained using instantaneous velocity fluctuation maps should ideally result in zero mean. However, in practice, the mean field obtained here reveals the discrepancy inherent in the mean velocity field estimated via adaptive ensemble binning. As necessary, this error is reported along with velocity profiles presented later. Furthermore, the uncertainty errors associated with other flow quantities reported in the present work are obtained according to the estimation procedure outlined in Appendix B.1.

AGW method is unaware of the flow physics involved, and despite that issue, it provides results with comparable accuracy to VIC#. Figure 2 illustrates a comparison of Reynolds stress component profiles within Zone3 obtained using different methods. The adaptive Gaussian weighting (AGW) method exhibits remarkable agreement with the results acquired through ensemble binning (EB). Upon detailed examination, data obtained through AGW appear slightly higher than that of EB attributing to top-hat filtering effect experienced in EB method (as discussed in the previous section). Figure 2 also features mean profiles obtained using VIC#, currently considered as a state-of-the-art regularization technique, at the same grid location showing excellent agreement with the computationally inexpensive AGW technique. However, a clear rationale explaining the discrepancy for spanwise stress profiles between AGW and VIC# remains elusive. It could be attributed to VIC# enforcing

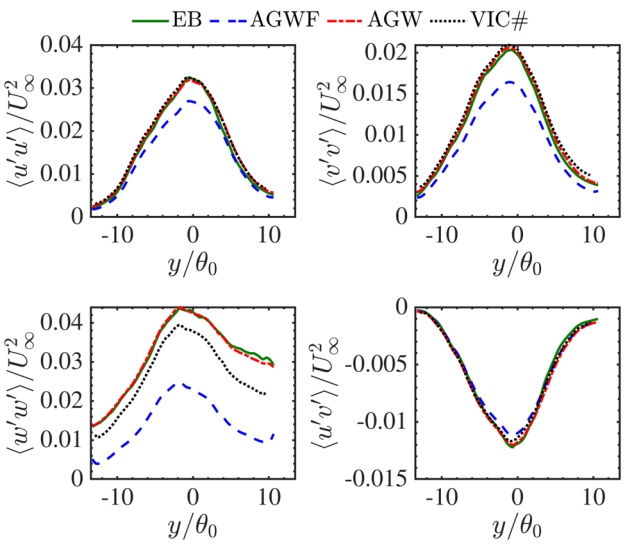


**Fig. 2** Comparison of mean stress profiles, $\langle u_i' u_j' \rangle$ within Zone3 obtained through ensemble binning (EB), adaptive Gaussian weighting (AGW), adaptive Gaussian weighting-filtered (AGWF), and Vortex-In-Cell (VIC#)

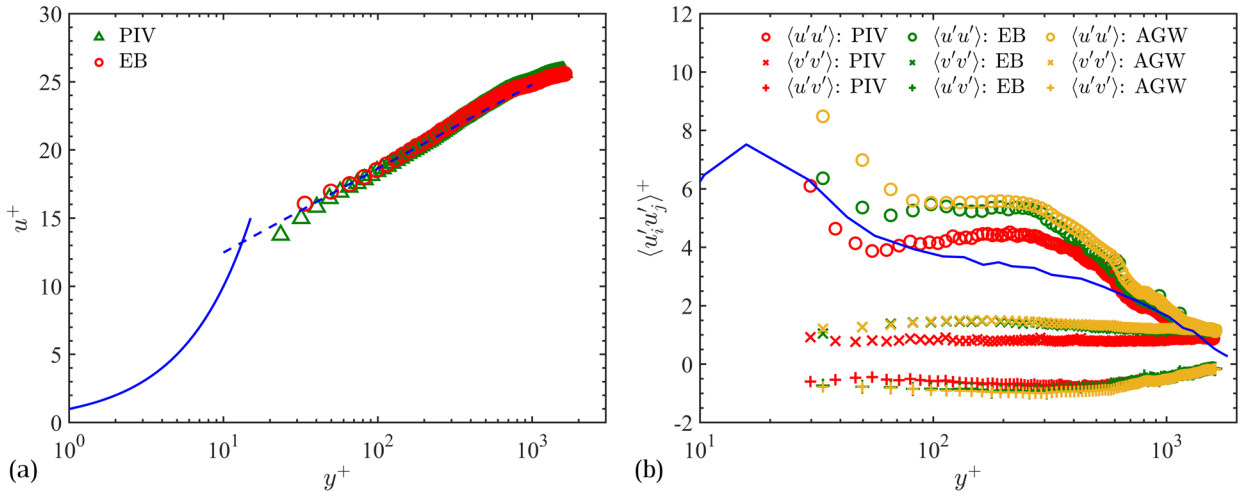


**Fig. 3** **a** Streamwise velocity profile in wall units. (○ EB, △ PIV): experimental measurements upstream of backwards-facing-step at $x/\theta_0 = -7.35$. (−−): logarithmic law of the wall, $u^+ = (1/\kappa)\ln y^+ + B$, with $\kappa = 0.37$ and $B = 6.31$. **b** Mean stress, $\langle u_i'u_j'\rangle^+$ profiles at $x/\theta_0 = -7.35$ ($x = -13.8$mm) obtained using PIV, EB, and AGW. Streamwise stress, $\langle u_i'u_j'\rangle^+$ profile from Morris and Foss (2003) (−: solid blue line) is shown for comparison

physical constraints, thereby eliminating measurement errors associated with PTV points, i.e., manifested in the EB and AGW profiles. Alternatively, this difference might point to a limitation of VIC# (DaVis—LaVision) in obtaining accurate spanwise fields.

Besides, the data represented by AGWF (adaptive Gaussian weighting-filtered) are the mean stress profiles obtained using all realizations of instantaneous velocity fluctuation maps, acquired through AGW, revealing substantial filtering effects. This significant difference arises because AGW has a greater filtering effect when using neighboring fluctuating velocity PTV points to interpolate stress components than on the preferable alternative to use local stress derived at the PTV points for grid interpolation. Thus, the spanwise component, $\langle w'w'\rangle$, is particularly affected due to the larger local variation in the spanwise velocity fluctuation, $w'$, compared to other components.

AGW being considerably competent in wall-free region, its accuracy near the wall region of boundary layer, where flow regions have significant velocity gradients and sparser particle number density, is expected to be lower. To validate and substantiate the near-wall data, we performed time-resolved adaptive-PIV (DaVis 10.2, LaVision Inc.) over the images captured by the camera directly facing the flow volume (Cam 1, refer to Fig. 1). We acknowledge that implementing 2D-PIV over a relatively thick flow region (∼ 6 mm) is not standard practice as in-plane measurements are subjected to larger perspective error (Lee et al 2022); hence, the PIV results only serve as an alternative method to compare the results obtained using the hybrid method combining EB and AGW.

### 3.3 Vortex identification Δ criterion

A vortex identification criterion based on $\Delta = (\frac{1}{2}R)^2 + (\frac{1}{3}Q)^3$, where $Q$ and $R$ are the second and third invariants of the velocity gradient tensor, is utilized to identify vortical regions in the flow (Chong et al 1990). According to critical point theory, $\Delta > 0$ corresponds to vortical regions where the velocity gradient tensor has complex eigenvalues. Two positive values for Δ, very close to each other, are used to obtain the iso-surfaces shown in Figs. 4 and 6. This choice is made to enhance the morphological details of coherent motion. Moreover, a local 3D-Gaussian filter is implemented

**Table 2** Flow parameters calculated at $x/\theta_0 = -7.35$

| Flow parameter | Value |
|---|---|
| Free-stream velocity, $U_\infty$ (m/s) | 1.37 |
| Friction velocity, $u_\tau$ (m/s) | 0.0532 |
| BL thickness, $\delta_{99\%}$ (mm) | 23.4 |
| Momentum thickness, $\theta_0$ (mm) | 1.88 |
| Displacement thickness, $\delta^*$ (mm) | 2.43 |
| Shape factor | 1.29 |
| $\mathrm{Re}_h = U_\infty h_c/\nu$ | 68 260 |
| $\mathrm{Re}_\tau = u_\tau \delta_{99\%}/\nu$ | 1 240 |
| $\mathrm{Re}_\theta = U_\infty \theta_0/\nu$ | 2 566 |

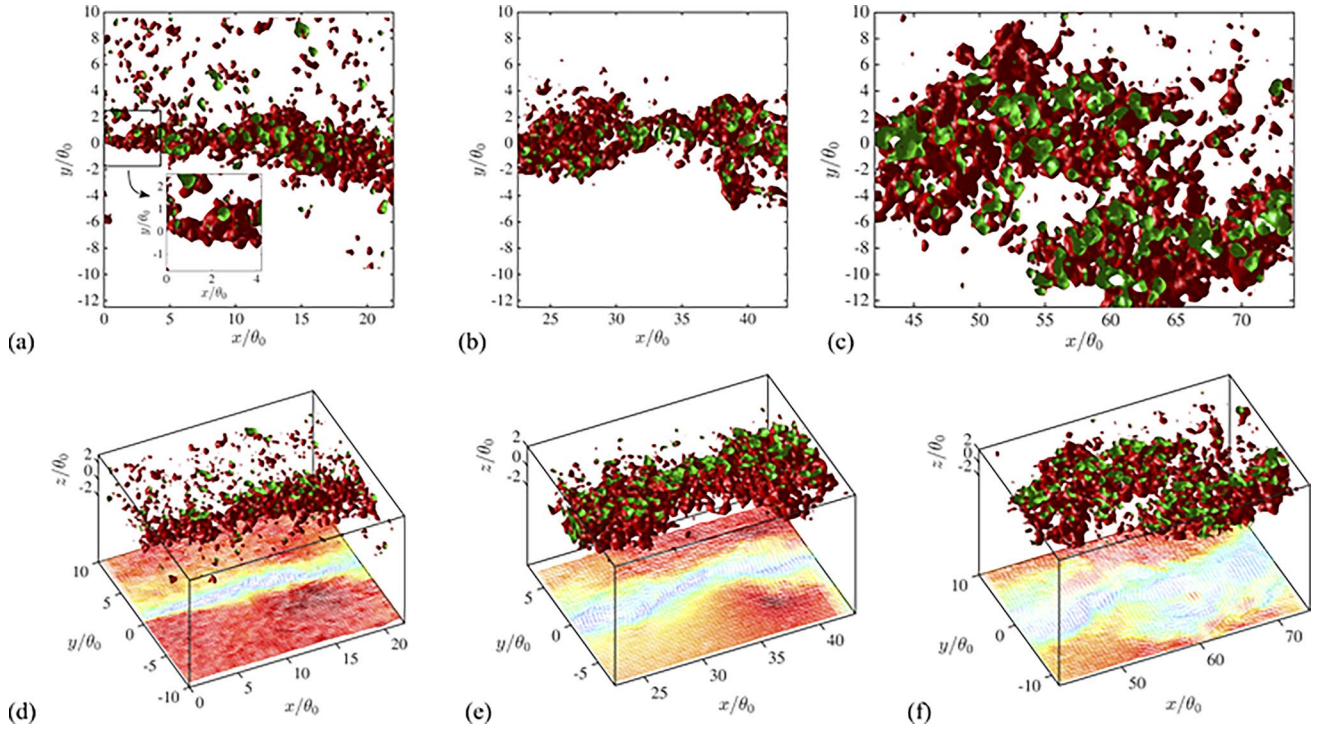


**Fig. 4** 2D projection *(top row)* and 3D *(bottom row)* rendering of instantaneous iso-surfaces for $\Delta = (2 \pm 0.5) \times 10^{12}$ in **a**, **d** Zone1 and **b**, **e** Zone2, and $(2 \pm 0.5) \times 10^{11}$ in **c**, **f** Zone3. Slightly larger and smaller values for $\Delta$ are assigned to two different colors to enhance the visibility of the flow morphology. 3D iso-surfaces accompany instantaneous Galilean-transformed 3D velocity (spanwise-averaged) vector plots colored by velocity magnitude to highlight the circulation region corresponding to the coherent motions

to clear out noise that cannot be unambiguously considered part of coherent motion.

## 4 Results and discussion

### 4.1 Initial boundary layer

The bulk-flow Reynolds number before the backward-facing step is $\mathrm{Re}_h = U_\infty h_c/\nu \approx 6.83 \times 10^4$, where $h_c$ is the half-tunnel height. At an upstream position of $x/\theta_0 = -7.35$ ($x = -13.8$ mm) from the separation edge, where $\theta_0$ =1.88 mm, is the initial momentum thickness at the bottom wall of the tunnel. The relevant boundary layer flow parameters are compiled in Table 2. Since $\mathrm{Re}_\tau = u_\tau \delta_{99\%}/\nu \approx 1\,240 > 700$, this is a high Reynolds number boundary layer (Jiménez et al 2010).

The primary purpose of the wall boundary flow characterization is to establish the initial flow condition for the mixing layer. The average streamwise velocity profile in the boundary layer at $x/\theta_0 = -7.35$, upstream of the backward-facing step, is shown in Fig. 3a. A first approximation to the origin of wall-normal coordinates is determined directly from laser reflections at the bottom surface of the tunnel. The modified Clauser chart method (Mejia-Alvarez 2010; Dixit and Ramesh 2009; Schultz and Flack 2007; Perry and Li 1990; Clauser 1954, 1956) is used to determine the friction velocity $u_\tau$, and to correct the origin of the wall-normal coordinate for small uncertainties. Subsequently, the logarithmic law of the wall is least-square fitted to the data to determine its constants as follows: von Kármán constant, $\kappa = 0.37$, and the intercept, $B = 6.31$. These values serve as a sanity check for the mean velocity profile of the approaching boundary layer because they are consistent with accepted values for smooth-wall turbulent boundary layers (Schlichting and Gersten 2000). The free-stream turbulence intensity, $u'/U_\infty$, is estimated to be $\approx 4\%$.

Figure 3a also shows velocity profiles obtained using both EB and 2D-PIV. As mentioned before, adaptive 2D-PIV data only serve as an alternative method to compare with AGW. The velocity profiles exhibit excellent agreement except for the grid point located closest to the wall. The turbulence stress profiles shown in Fig. 3b also include AGW data along with EB and 2D-PIV. The EB and AGW methods demonstrate substantial agreement, except in the vicinity of high-velocity gradients, i.e., near the wall where the EB method tends to underestimate the values due to more pronounced top-hat filtering effects. On the other hand, 2D-PIV exhibits

lower values for all stress profiles as the method is sensitive to the flow direction and spatial filtering effects, specially in wall-normal direction. In comparison with the streamwise stress profile of Morris and Foss (2003) (blue solid line), the profiles show a distinct hump accredited to relatively high free-stream turbulence intensity, ≈ 4%. On a different note, VIC# calculations (DaVis—LaVision) at the same grid location (not shown herein) displayed significant deviations near the wall region from the profiles in Fig. 3a,b, raising concerns about the reliability of the VIC# package included with DaVis 10.2 (LaVision Inc.) in regions of extreme velocity gradients.

### 4.2 Transition from boundary layer to shear layer

For $x/\theta_0 \lesssim 5$, we observe relatively smoother coherent motion with an initial Kelvin–Helmholtz (KH) instability roll-up of the order of the initial momentum thickness, $\theta_0$ (Fig. 4a,d). This high-strain region of the flow, as previously reported by Morris and Foss (2003), is viscous-dominated and can be attributed to the sudden shutdown of the stress-inducing (or turbulence production) source in the flow (i.e., the wall), resulting in rapid energy dissipation immediately downstream of the edge. Nevertheless, the instability of the inflectional velocity profile across the interface of the two streams, compounded with the inherent shear instabilities, transitions the flow to a turbulent regime, overcoming the viscous-dominated region. We discuss this further from the viewpoint of the turbulent kinetic energy budget in Sect. 4.5. Further downstream, coherent motions begin to deform increasingly to attain a higher degree of three-dimensionality in addition to the gradual increase in the population of small-scale coherent motions.

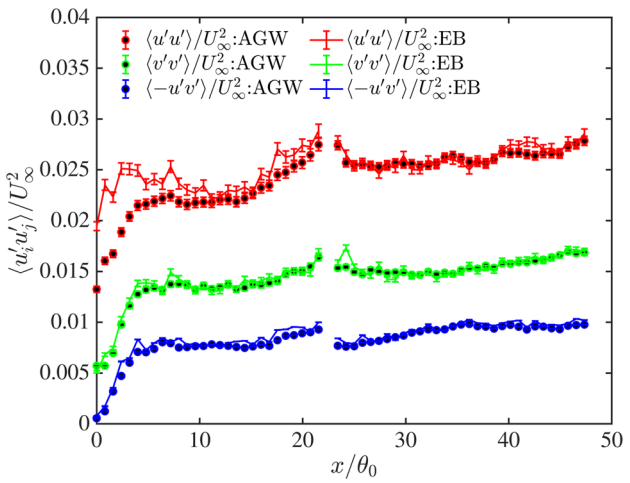


**Fig. 5** Peak mean stress variation along streamwise locations, x/$\theta_0$ covering Zone1 and Zone2

The characteristics of the viscous-dominated region are consistent with the rapid increase in the peak of mean stress shown in Fig. 5. Beyond the separation point, streamwise Reynolds normal stress, $\langle u'u'\rangle$, shows the largest value, a contribution of both streamwise stresses translating from the BL region onto the immediate downstream of the edge and the "flapping" motion of the shear layer. The cross-stream stress component, $\langle v'v'\rangle$, and the Reynolds shear stress, $\langle -u'v'\rangle$, displayed comparable values within the BL; however, upon separation the rapid stream adjusts to a new "boundary-free" condition as Reynolds stresses distribute in the other two directions, evident from the gradual increase in normal and shear stress components' peak stress. The peak streamwise and cross-stream stress appears to reach a local minimum around $x/\theta_0 \approx 12$, suggesting a transition from a viscous-dominated region to a more active turbulence production region from this location onward. Comparable trends in local minimum of velocity RMS fluctuation magnitude are noted by Morris and Foss (2003) (refer to their Fig. 15), reinforcing our shared conclusion regarding the presence of a viscous-dominated region immediate downstream to separation. Furthermore, the transition from this region to an active production zone finds support through a turbulent kinetic budget analysis in the region, detailed in Sect. 4.5.

Transitioning to a turbulent regime creates clear morphological changes within the mixing layer. Figure 4 shows that distinguishable larger vortical coherent motions appear downstream of $x/\theta_0 \gtrsim 5$. Consistent with KH roll-ups induced by the primary instability in the upstream flow, as the shear layer develops, the coherent motions exhibit organized behavior and grow larger as they entrain the surrounding fluid from high- and zero-speed streams. Furthermore, these organized coherent motions are often accompanied by low momentum zones devoid of eddies between the vortical coherent motions. The shear layer width primarily grows by the "nibbling" action of small-scale vortices near the edges and "engulfing" action by large-scale vortices (Brown and Roshko 1974; Taveira et al 2013), though occasionally, the organized vortices exhibit mutual interaction. This interaction process leads to vortex pairing and the growth of mixing layer width. Figure 6 captures and shows one such vortex pairing event.

Figure 6 shows iso-surfaces obtained using Δ-criterion to illustrate the evolution of the pairing process between vortices of unequal strengths. The 3D iso-surfaces are accompanied by Galilean-transformed 3D vector plots (spanwise-averaged) colored by local velocity magnitude (color transitioning from blue to red corresponding to lowest and highest velocity, respectively) to highlight the circulation region corresponding to the vortical structures, and saddle region correlated to braids. In the first step (see Fig. 6a), two large-scale vortices (light blue ellipses) connected by a braid

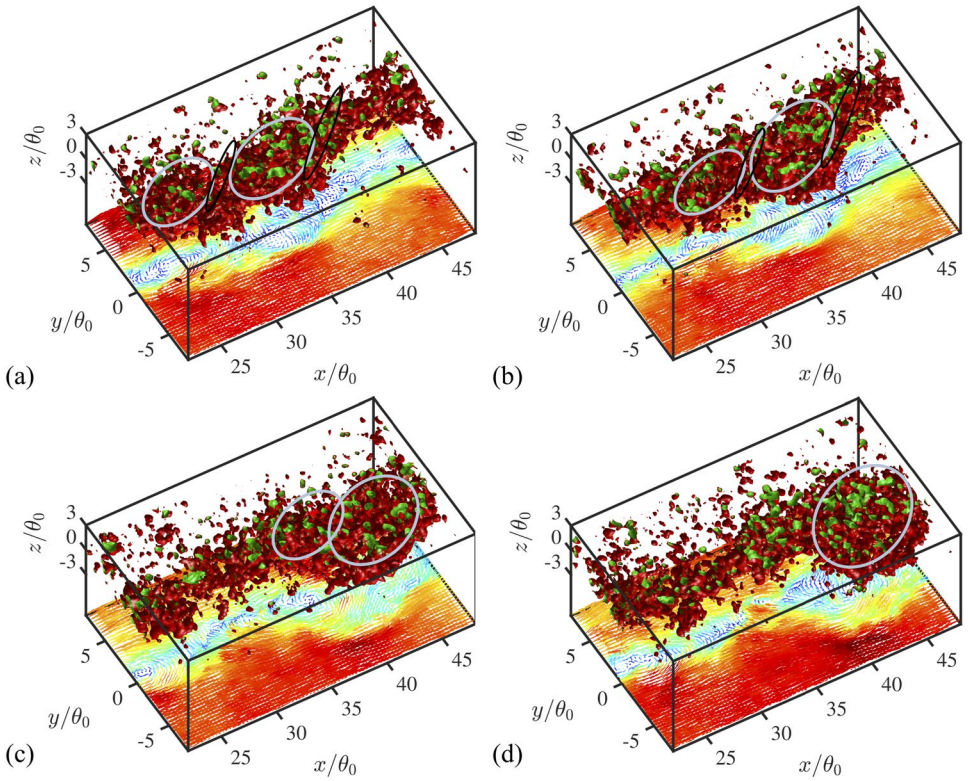


**Fig. 6** 3D rendering of instantaneous iso-surfaces for $\Delta = (2 \pm 0.5) \times 10^{12}$ depicting vortex pairing within Zone2 for time stamp, t = 0 (a), 10 ms (**b**), 31.25 ms (c), 42.75 ms (d) accompanied by instantaneous Galilean-transformed 3D velocity (spanwise-averaged) vector plots. Notice the two KH roll-ups of unequal strengths (light blue ellipses) with braids (black ellipses) pair as they develop. Access the supplementary multimedia file online for the animation

(black ellipse) begin to show circumferential interaction. In the second step, a comparatively larger strain is observed at the interface of the two vortices resulting in mutual vortex stretching (Fig. 6b,c), followed by an amalgamation of both of the vortices into one larger vortex (Fig. 6d).

Besides, the streamwise separation between the roll-ups increases downstream except in the event of the vortex pairing process. While the KH roll-ups are spanwise-dominant, an increase in the three-dimensionality of the flow is noticed in the vortices' deformed and stretched elliptical shape. A larger population of small-scale eddies is observed in Zone3; however, these smaller eddies are confined within larger vortices connected by braids. The large vortices and the braids appear to be two-dimensional; however, given the relatively smaller spanwise extent of the flow region, we refrain from providing a factual inference. Nonetheless, a considerable two-dimensional behavior of the braids at a relatively lower Reynolds number is observed by Browand and Troutt (1985); Lasheras et al (1986); McMullan and Garrett (2016) over a comparatively sizeable spanwise extent.

Past studies (Brown and Roshko 1974; Hussain and Zaman 1985) have observed self-similar regions to be devoid of classical pairing. However, recent work of Baltzer and Livescu (2020) has confirmed the occurrence of pairing events even in self-similar regions, supporting the indications made by Rogers and Moser (1994). No such pairing events, if any, are observed in Zone3 due to the limited streamwise dimensions of Zone3 relative to the growing size of spanwise roll-ups (Fig. 4c,f). Thus, a statistical evaluation is performed to more faithfully test the presence of self-similarity.

### 4.3 Shear layer growth

As discussed, the vortical coherent motions within the shear layer "engulf" and "nibble" on the surrounding fluid. As the entrainment increases, the layer spreads in the cross-stream direction downstream. Following Pope (2000), the width of the shear layer, $\delta$, at a streamwise location is defined as the distance between the cross-stream locations, $y_{0.9}$ and $y_{0.1}$, where the streamwise velocity reaches $U(y_{0.9}) = (U_l + 0.9U_s) \pm 0.01U_s$ and $U(y_{0.1}) = (U_l + 0.1U_s) \pm 0.01U_s$, respectively. Here, $U_s = U_h - U_l$, and $U_h = U_\infty$ and $U_l = 0$ are high- and low-speed stream velocities, respectively. The uncertainty value of $\pm 0.01U_s$ is adopted to account for the data binning process over the structured grids of finite size. The locus of $y_m$, the mixing layer mid-plane, is obtained as $y_m = 0.5(y_{0.9} + y_{0.1})$ and $y_{0.5}$ corresponds to the cross-stream location where streamwise velocity attains convection velocity, $U(y_{0.5}) = U_c = (U_l + 0.5U_s) \pm 0.01U_s$, or $U(y_{0.5}) = \frac{U_h + U_l}{2} = 0.5\,U_\infty$.

Linear growth of a shear layer is widely regarded as a necessary condition for self-similarity. The variation of the

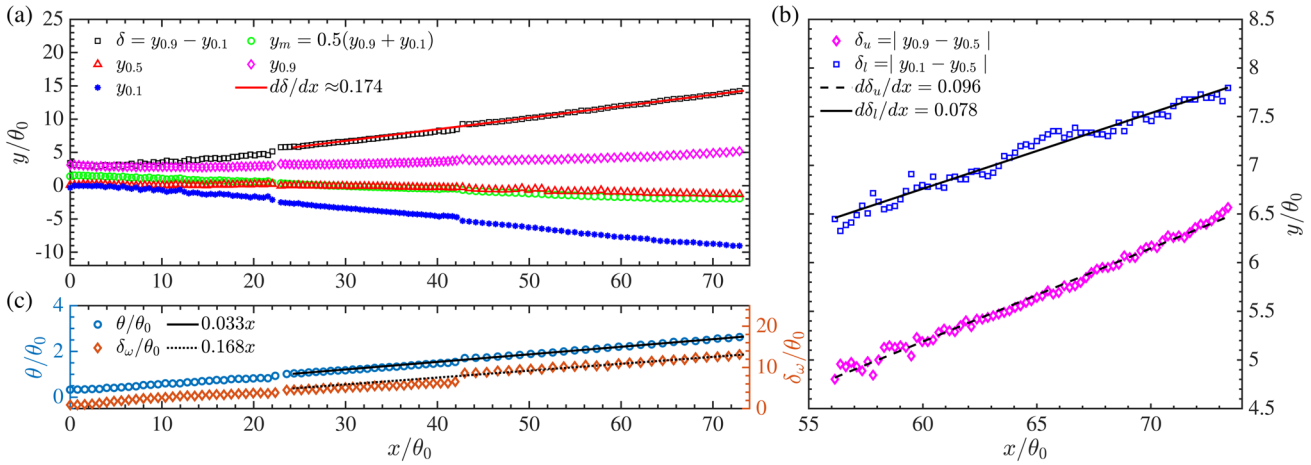


**Fig. 7** **a** Variation of shear layer width $\delta$ and cross-stream locations of $y_{0.1}, y_m, y_{0.9}$ and $y_{0.5}$ (as defined in 4.3) of the shear layer along the streamwise direction. **b** Growth of upper and lower edges relative to the shear layer centerline, $y_{0.5}$. **c** Momentum thickness, $\theta$, and vorticity thickness, $\delta_\omega$ variation along streamwise direction

shear layer width, $\delta$, along the streamwise direction is shown in Fig. 7a for the present study. A least-square linear fit is performed only over the self-similar region (discussed in the next section). The SSSL width, $\delta$, grows linearly at a rate of $d\delta/dx \approx 0.174$ for $\frac{x}{\theta_0} \gtrsim 20$. A normalized quantity defined as spreading rate, $S = \frac{U_c}{U_s}\frac{d\delta}{dx}$ (Pope 2000), is estimated to be $S \approx 0.087$ in the present study, comparable to previously reported values of $S = 0.085$ (Liepmann and Laufer 1947) and $S = 0.104$ (Champagne et al 1976) for planar SSSL, $0.079 \leq S \leq 0.085$ (initial laminar condition) and $0.093 \leq S \leq 0.101$ (turbulent initial condition) (Hussain and Zedan 1978b) for axisymmetric SSSL. However, the growth rate is comparatively higher than TSSL reported in the literature, i.e., $0.06 \leq S \leq 0.11$ (Dimotakis 1991), $S = 0.069$ (Bell and Mehta 1990; Balamurugan et al 2020; Baltzer and Livescu 2020), and $S = 0.062$ (Rogers and Moser 1994), but it is consistent with the variation of the growth rate with the normalized velocity difference, $\lambda = (U_h - U_l)/(U_h + U_l)$, found in previous studies (Wei et al 2022).

In the same plot, we show the variation of $y_{0.1}$, $y_m$, $y_{0.9}$, and $y_{0.5}$. The loci of $y_{0.5}$ and $y_m$ do not overlap for $x/\theta_0 \lesssim 20$, attributing to the developing phase of the shear layer. For $x/\theta_0 \gtrsim 30$, the locus of convection velocity, $U_c$ (or $y_{0.5}$), lies on the high-speed side of the mixing layer centerline, thus disagreeing with the locus of $y_m$. This provides evidence to difference in growth behavior of upper and lower edge of the shear layer, discussed further in subsequent paragraph. Besides, a least-square fit (not shown in Fig. 7a) yields a slope of $\approx -0.029$ for $y_{0.5}$ in the self-similar region that is similar to the reported values of $-0.031$ (Liepmann and Laufer 1947) and $-0.035$ (Champagne et al 1976) for an SSSL. We use $y_{0.5}$ to obtain the similarity parameter, $\xi$, as opposed to the parameter $y_m$ used in Pope (2000). We believe $y_{0.5}$ to be a more appropriate scaling parameter here as it corresponds to the convection velocity, $U_c$. This is also consistent with the more general self-similarity analysis outlined in Wei et al (2022). It is worth pointing out that the locus of maximum Reynolds shear stress (not shown herein) does not overlap with $y_{0.5}$ and is found to be biased toward the high-speed side of the centerline.

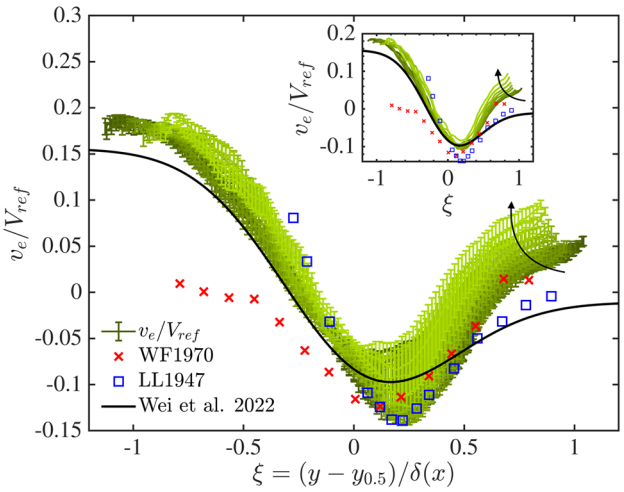


**Fig. 8** Normalized cross-stream velocity profiles with error bars ($v_e/V_{\text{ref}}$) within the self-similar region ($55 \lesssim x/\theta_0 \lesssim 73$), progressively transitioning from darker to brighter shades of green along the displayed arrow, spaced by $x = 1.91\theta_0$. Profiles obtained by Liepmann and Laufer (1947) (□, LL 1947) and Wygnanski and Fiedler (1970) (×, WF 1970), and entrainment velocity profile obtained using equation 4 as suggested by Wei et al (2022) (−) are shown for comparison. Inset shows the identical cross-stream velocity profiles without the error bars

The shear layer centerline, $y_{0.5}$, inclines toward the zero-speed stream, indicating the mixing asymmetry, consistent with past studies (e.g., Koochesfahani et al (1983); Grinstein et al (1986); Liepmann and Laufer (1947); Champagne et al (1976); Wei et al (2022)). The downward penetration of the high-speed stream is evident from the larger width of the lower edge ($\delta_l$) relative to the centerline as compared to the upper edge $\delta_h$, shown in Fig. 7b. The widths, $\delta_u$ and $\delta_l$, correspond to the absolute $y$-distance between the SSSL's centerline, $y_{0.5}$, and upper and lower edges, respectively. It is only shown for Zone3 as it encompasses the self-similar region (further details on self-similarity in Sect. 4.4). In addition to the obvious asymmetry, the upper edge of the shear layer, $\delta_u$, grows at a rate of $d\delta_u/dx = 0.096$, i.e., faster than the lower edge, $\delta_l$ growing at a rate of $d\delta_l/dx = 0.078$, contrasting with the observations of Balamurugan et al (2020); Champagne et al (1976).

On the other hand, the cross-stream velocity profile (refer to Fig. 8) indicates a larger velocity (pointing toward the SSSL centerline) on the zero-speed-stream side than the high-speed-stream side (velocity vector pointing away from the centerline), indicating higher entrainment from the zero-speed stream. While large-scale coherent motions dictate statistics concerning entrainment rates presented in Fig. 7, fluid entrainment in shear layers occurs primarily ($\approx 99\%$ Taveira et al (2013)) through the "nibbling" action of small flow scales rather than the "engulfing" action of large-scale coherent motions (Mathew and Basu 2002; Taveira et al 2013). A strong correlation of enstrophy change with enstrophy viscous diffusion is observed by Taveira et al (2013), concluding the dominant role of small flow scales in the entrainment mechanism. Hence, a higher growth rate of the upper edge of SSSL can be attributed to the comparatively higher free-stream turbulence intensity ($\approx 4\%$) in the primary stream, evidence for which is also provided by Hussain and Zedan (1978a). The elevated turbulence levels lead to higher enstrophy exchange at the upper edge of SSSL which could be the reason behind relatively larger positive cross-stream velocity magnitude near this location. At the same time, the enstrophy produced within the shear layer is responsible for mixing the engulfed fluid from the irrotational zero-speed-stream side. We provide further discussion in Fig. 8 in the next section.

Streamwise growth of momentum thickness ($\theta$) and vorticity thickness ($\delta_\omega$) are statistical quantities of interest for a mixing layer characterization. Both quantities show linear growth behavior in Zone2 and Zone3; see Fig. 7c. The momentum thickness grows with a consistent slope of $d\theta/dx \approx 0.033$ for $x/\theta_0 \gtrsim 25$, though the least-square fit is performed over the identified self-similar region ($55 \lesssim x/\theta_0 \lesssim 73$, more discussion in next section). The observed growth rate of momentum thickness is consistent with previously reported values for SSSL $d\theta/dx = 0.035$ (Morris and Foss 2003), $d\theta/dx = 0.032$ (Hussain and Zaman 1985), $d\theta/dx = 0.033$ (Rajagopalan and Ko 1996). The vorticity thickness as well displays linear growth at a rate of $d\delta_\omega/dx \approx 0.168$ comparable to the reported values of $d\delta_\omega/dx = 0.145$ (Patel 1973), $d\delta_\omega/dx = 0.17$ (Wygnanski and Fiedler 1970), $d\delta_\omega/dx = 0.202$ (Mills 1968), and $d\delta_\omega/dx = 0.218$ (Liepmann and Laufer 1947), though a relatively large dispersion exists among the data.

Brown and Roshko (1974) performed various fitting procedures on data from the literature (cf. Fig. 10) to obtain a "universal" scaling for vorticity thickness, $\delta_\omega$ growth. Their fitting techniques resulted in scaling that varied in the range $0.162$–$0.181\lambda$, for $\lambda = (U_h - U_l)/(U_h + U_l)$ ranging from 0.1 to 1. These scalings show reasonable agreement with the TSSL scaling found by Browand and Latigo (1979); Browand and Troutt (1985); D'Ovidio and Coats (2013), which fall in the range $0.15$–$0.17\lambda$. The present results, $0.168\lambda$, fall into the suggested range as well. However, unlike Brown and Roshko (1974), the studies of Browand and Latigo (1979); Browand and Troutt (1985); D'Ovidio and Coats (2013) do not include growth data corresponding to SSSL (i.e., $\lambda = 1$) to obtain the "universal" scaling. Besides, the fitting performed by Brown and Roshko (1974) showed a large root mean square deviation among the growth rates for SSSL found in the literature at that time. To this date, an inclusive scaling for the growth of SSSL and TSSL does not exist. This raises a few questions: Is it plausible that a fundamental difference exists in the spatial development of SSSL from TSSL, despite the former being the limiting case of the latter, i.e., $\lambda = 1$? Does there exist a growth rate scaling that unifies both flows beyond a reasonable doubt? Thus, there is an impending need to obtain a universal growth scaling incorporating SSSL and TSSL.

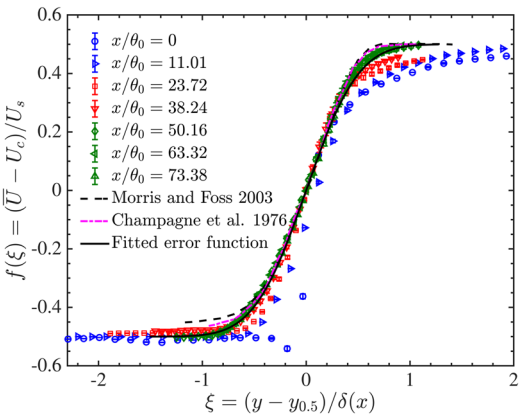


**Fig. 9** Scaled velocity profiles, $f(\xi)$ at different $x/\theta_0$ superimposed with SSSL profiles obtained by Morris and Foss (2003) (– – –) and Champagne et al (1976) (— · —). (–): error function $f(\xi) = \frac{1}{2}\,\mathrm{erf}\left[\frac{\xi}{\sigma}\right]$ where $\sigma = 0.5522$, fitted over the scaled velocity profiles across the self-similar region $55 \lesssim x/\theta_0 \lesssim 73$

We present the mean velocity characteristics and higher-order turbulence quantities in the following section to further evaluate self-similarity in the flow region.

### 4.4 Self-similar region

The statistical descriptors of turbulence for a mixing layer attain self-similarity in the scaled flow coordinates (Pope 2000), i.e., the statistical descriptors become independent of the streamwise location. The scaled streamwise velocity at several locations within Zone1 to Zone3 is shown in Fig. 9. The profiles collapse reasonably well for $x/\theta_0 > 50.16$, i.e., throughout Zone3 (green symbols in Fig. 9). However, the collapse of the mean velocity profiles is a necessary but not sufficient condition to identify the onset of self-similarity, as higher-order statistics take a longer distance to exhibit collapsing (Mehta and Westphal 1986). The scaled velocity profile obtained by Champagne et al (1976) and Morris and Foss (2003) for an SSSL is also shown for comparison, which is in good agreement with the present results. The scaled velocity profiles in the self-similar region are often represented by an error function. Here, an error function, shown with solid line, is fitted through the velocity profiles for $55 \lesssim x/\theta_0 \lesssim 73$, i.e., the region identified as self-similar.

Figure 8 shows cross-stream velocity profiles normalized with $V_{\text{ref}} = U_\infty d\delta/dx$ (Wei et al 2022) for streamwise locations within the self-similar region ($55 \lesssim x/\theta_0 \lesssim 73$). The profiles show reasonable convergence within measurement uncertainty and compare well with the hot-wire measurements of Liepmann and Laufer (1947) and Wygnanski and Fiedler (1970). Additionally, Wei et al (2022), for plane mixing layers, suggested an entrainment velocity function (refer to Eq. 4) based on the error function fit for streamwise velocity profile in the self-similar region. Here, $B = \frac{dy_{0.5}}{dx} / \frac{d\delta}{dx}$, and $\sigma$ is obtained by fitting an error function to the streamwise velocity profile (refer to Fig. 9 caption). The cross-stream velocity profile obtained using Eq. 4 (solid black line) shows excellent agreement on the low-speed side of SSSL, while it noticeably diverges from the measured velocity profiles on the high-speed side. As discussed in preceding section, this discrepancy can be attributed to the heightened enstrophy exchange near the upper edge of the SSSL, causing increased cross-stream velocity. It is worth noting that Eq. 4 is purely analytical, based on mean statistical parameters, and does not account for non-ideal conditions such as current free-stream boundary conditions and confinement effects that influence the entrainment rate.

$$\frac{v_e}{V_{\text{ref}}} = \frac{B}{2}\text{erf}\left(\frac{\xi}{\sigma}\right) - \frac{\sigma}{2\sqrt{\pi}}e^{-\frac{\xi^2}{\sigma^2}} + \frac{\sigma}{2\sqrt{\pi}} + \frac{B}{2\lambda} \tag{4}$$

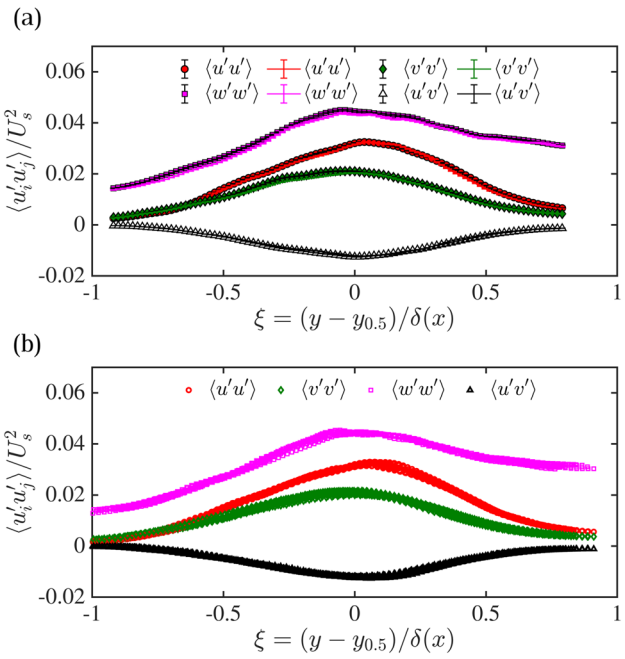


**Fig. 10** Cross-stream profiles of four components of the Reynolds stress tensor **a** at a location within Zone3 obtained by EB (solid lines) and AGW (symbols) shown for comparison; and **b** in the region $55 \lesssim x/\theta_0 \lesssim 73$ obtained using AGW sampled at streamwise intervals of size $x/\theta_0 = 0.239$ without streamwise averaging

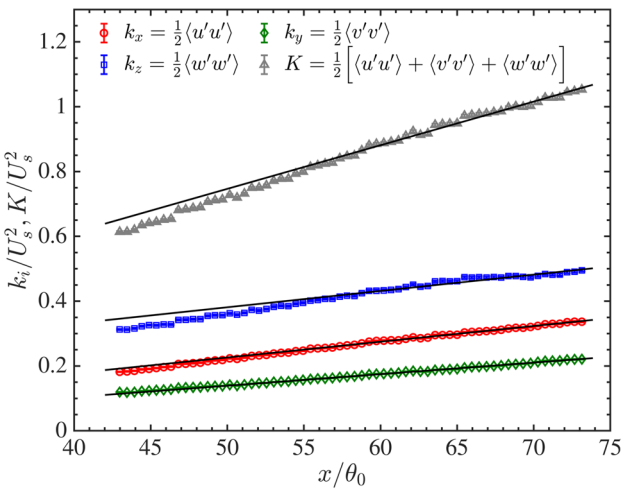


**Fig. 11** Variation of total turbulent kinetic energy ($K = \int_{-\infty}^{\infty} k_i \, dy$) and its individual components ($k_i = \frac{1}{2}\langle u_i' u_i' \rangle$) along the streamwise direction in Zone3. (Every second data marker is shown for clarity.) (−): linear least-squares fit for $x/\theta_0 \gtrsim 55$ (self-similar region)

Higher-order statistical descriptors of turbulence, such as Reynolds stress components, are better indicators of self-similarity than the mean velocity profile because of their

**Table 3** Relevant turbulence flow parameters calculated over the self-similar region, i.e., $55 \lesssim x/\theta_0 \lesssim 73$ of the SSSL. The uncertainty bounds show the extent of variability of each quantity across the self-similar region

| Turbulence flow parameter | |
|---|---|
| Dissipation rate, $\epsilon$ | 0.065±0.022 $m^2/s^3$ |
| Kolmogorov length-scale, $\eta = \left(\frac{\nu^3}{\epsilon}\right)^{1/4}$ | 64±6 $\mu$m |
| Kolmogorov time-scale, $\tau_\eta = \left(\frac{\nu}{\epsilon}\right)^{1/2}$ | 4.1±0.80 ms |
| Taylor microscale, $\lambda_T = \sqrt{\left(\frac{15\nu}{\epsilon}\right)} \cdot \langle V' \rangle_{\text{rms}}$ | 2.9±0.18 mm |
| Taylor Reynolds number, $Re_{\lambda_T} = \frac{\langle V' \rangle_{\text{rms}} \lambda_T}{\nu}$ | 543.5±143.5 |

$\langle V' \rangle_{\text{rms}} = \sqrt{\left(\langle u'^2 \rangle + \langle v'^2 \rangle + \langle w'^2 \rangle\right)/3}$

higher sensitivity to changes in flow conditions (Rogers and Moser 1994; Attili and Bisetti 2012). Figure 10a shows cross-stream profiles of four components of the Reynolds stress tensor gained by AGW (symbols) and EB (solid lines) at a single grid point within the self-similar region that again highlights the minimal discrepancy between the two methods. Figure 10b illustrates the collapse of profiles sampled along the streamwise coordinate at intervals of size $x/\theta_0 = 0.239$ in the region $55 \lesssim x/\theta_0 \lesssim 73$. There is no streamwise averaging in these profiles to show their streamwise variability. These Reynolds stress profiles show excellent collapse over the observed flow region, suggesting that the flow has attained self-similarity. The peaks of Reynolds stresses occur on the high-speed stream side of the mixing layer, consistent with the claim of peak stress not coinciding with the cross-stream location of the centerline ($y_{0.5}$). A number of turbulent flow parameters calculated in the self-similar region are tabulated in Table 3.

To further validate the assessment of self-similarity, we show the streamwise evolution of individual components of turbulent kinetic energy (TKE) and the total TKE integrated across the cross-stream direction in Fig. 11. The total kinetic energy and its individual components growth exhibit linear behavior for $x/\theta_0 \gtrsim 55$, further validating our assessment that the flow has attained self-similar behavior (Attili and Bisetti 2012).

### 4.5 Turbulent kinetic energy budget

The turbulent kinetic energy (TKE) budget is obtained across critical regions of the shear layer. The individual terms of the TKE budget equation are obtained using the general form of the equation as follows (Liu and Thomas 2004):

$$\underbrace{\frac{\partial k}{\partial t}}_{\text{Temporal Term}} = \underbrace{-\overline{U_i}\frac{\partial k}{\partial x_i}}_{\text{Convection Term}} \underbrace{-\frac{\partial}{\partial x_i}\overline{u_i'\left(\frac{p'}{\rho}\right)}}_{\text{Pressure Diffusion}} \underbrace{-\frac{\partial}{\partial x_i}\overline{u_i'k'}}_{\text{Turbulence Diffusion}} \underbrace{-\overline{u_i'u_j'}\frac{\partial \overline{U_j}}{\partial x_i}}_{\text{Production}} + \underbrace{\nu\frac{\partial}{\partial x_i}\overline{u_j'\left(\frac{\partial u_i'}{\partial x_j} + \frac{\partial u_j'}{\partial x_i}\right)}}_{\text{Viscous Diffusion}} \underbrace{-\overline{\nu\left(\frac{\partial u_i'}{\partial x_j} + \frac{\partial u_j'}{\partial x_i}\right)\frac{\partial u_j'}{\partial x_i}}}_{\text{Dissipation}} \tag{5}$$

where $\nu$ is kinematic viscosity, $k = \frac{1}{2}\overline{u_i'u_i'}$ is mean TKE, and $k' = \frac{1}{2}u_i'u_i'$ is fluctuating TKE. $u_i'$ and $\overline{U_i}$ are fluctuating and mean velocities, respectively. The temporal term on the left-hand side of the equation is zero under statistically stationary flow conditions. The pressure diffusion term is not obtained in the present study; nonetheless, its absence does not alter the physical inferences discussed in the subsequent text.

The production term in equation 5 consists of nine individual components. The magnitude and sign of the dictating terms collectively decide the sign for the production term. As discussed in Sect. 4.2, the region immediately downstream of the separation point exhibits a relatively large magnitude of streamwise stress, $\langle u'u' \rangle$ upon emanating from the near-wall region of the BL (see Fig. 5). Additionally, the flow attached to the boundary layer suddenly loses the no-slip condition, resulting in a large streamwise gradient of streamwise velocity, $\frac{\partial \overline{U}}{\partial x}$. The sudden flow expansion at the separation edge indicates longitudinal stretching of the streamwise velocity, consistent with the large streamwise Reynolds normal stress, $\langle u'u' \rangle$ near the separation edge. The joint contribution of the above two terms primarily results in considerable negative production immediate downstream to the separation edge, refer to Fig. 12a. The rest of the components of the production term are two orders of magnitude smaller than $-\langle u'u' \rangle \frac{\partial \overline{U}}{\partial x}$. It is worth pointing out that the cross-stream gradient, $\frac{\partial \overline{U}}{\partial y}$, is positive and higher in magnitude. However, Reynolds shear stress, $\langle -u'v' \rangle$, is comparatively smaller in the region, and the combined contribution of the term is negligible as a result. The negative production rate can be seen for $0 \leq x/\theta_0 \leq 0.80$ in Fig. 12a. Negative production rate implies that turbulence energy is being rapidly dissipated at a rate greater than it is generated in the region. This depicts the presence of laminar sublayer immediate to the separation edge. Additionally, the cross-stream profiles show decreasingly lower negative production rate

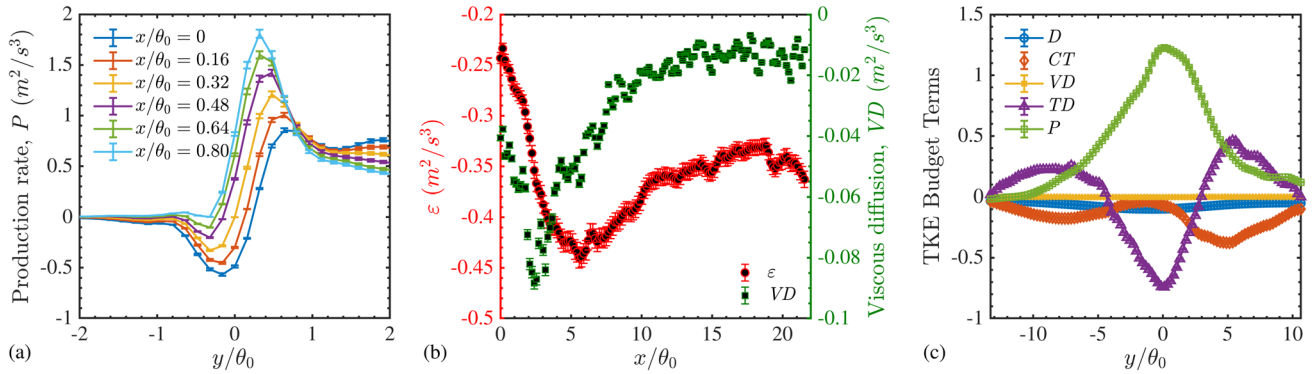


**Fig. 12** **a** Cross-stream profiles of production rate immediate to the separation edge ($0 \le x/\theta_0 \le 0.80$), **b** Streamwise variation of the peak minimum values in cross-stream profiles of dissipation rate ($\varepsilon$) and viscous diffusion rate. **c** Ensemble-average TKE budget obtained over the self-similar region ($55 \lesssim x/\theta_0 \lesssim 73$). *D*: Dissipation, *CT*: Convection Term, *VD*: Viscous Diffusion, *TD*: Turbulence Diffusion, and *P*: Production as labeled in equation 5

depicting the overcoming of the laminar behavior by the turbulence produced nearby.

A DNS study by Cimarelli et al (2019) found the production term to be negative near leading and trailing separation edges, and flow reattachment zones, similar to the present observation. As an aside, the production term is always kept positive in turbulence models (e.g., eddy viscosity models). Such models can be improved by exercising the presence of negative production in the flow, particularly in separating flows.

Figure 12b presents the streamwise variation of the peak minimum values in cross-stream profiles of dissipation rate ($\varepsilon$) and the viscous diffusion rate, to illustrate the viscous-dominated region immediate downstream to the separation edge. The plot demonstrates a significant variation in both quantities for $x/\theta_0 \lesssim 12$, followed by minimal variation beyond this point. The variation is rather rapid for viscous diffusion rate than dissipation rate indicating its larger role in the redistribution of turbulent kinetic energy produced, thus establishing its dominating role in the laminar-like region immediate to the separation edge. Furthermore, dissipation rate magnitude also increases after separation reaching a maximum at $x/\theta_0 \approx 6$, which is consistent with the comparatively smoother flow morphology observed upstream of this location (see Fig. 4a, d).

The TKE budget in the self-similar region obtained over $55 \lesssim x/\theta_0 \lesssim 73$ is plotted in Fig. 12c. The production profile shows a slight bias for the high-speed stream side, similar to the stress profiles. The turbulence diffusion profile is skewed toward the zero-speed stream, as a larger turbulence diffusion from the high to zero-speed side prevails in the present SSSL. In the following section, a discussion on distribution of critical TKE budget terms within the coherent flow motions of the shear layer is provided.

### 4.6 Phase-averaged flow maps

The phase averaging method analyzes strong rotating coherent motions within a shear layer and obtains a mean flow map of these coherent motions. The process is adapted from the one described in Loucks and Wallace (2012) to identify instances of vortical coherent motions in Zone3 as it encompasses the self-similar region. The oscillating streamwise velocity signal at a fixed point on the zero-speed side of the SSSL indicates the presence of these large-scale vortical coherent motions. The instantaneous flow maps corresponding to specific streamwise velocity phases are identified to obtain the mean flow maps of velocity and other relevant turbulence flow quantities.

The time trace of the streamwise velocity displays alternating crests and troughs corresponding to the vortex center and the "braid" region between neighboring vortices. A fixed point is carefully selected to effectively capture both the vortex and braid region of the shear layer. Over the 12-second time trace, approximately 70 such local maxima or minima are identified. Given the limited number of detected events, additional instantaneous flow maps, 10 preceding and 10 following each crest or trough, are included in the ensemble (a total of 1 400 instantaneous flow maps) to produce a smoother flow map. The resulting average flow maps corresponding to the crest and trough phases are displayed in Fig. 13, with the left column representing the crest phase and the right column representing the trough phase. The dashed vertical black lines overlaid over the contour maps pass through the vortical core and saddle point within the braid region in the left and right columns, respectively.

Figure 13 shows the phase-averaged flow contour maps for different turbulence quantities. The frame of reference of the 2D velocity field is changed with a Galilean transformation based on the convection velocity, $U_c$. This velocity field is overlaid on the above-mentioned contour maps to

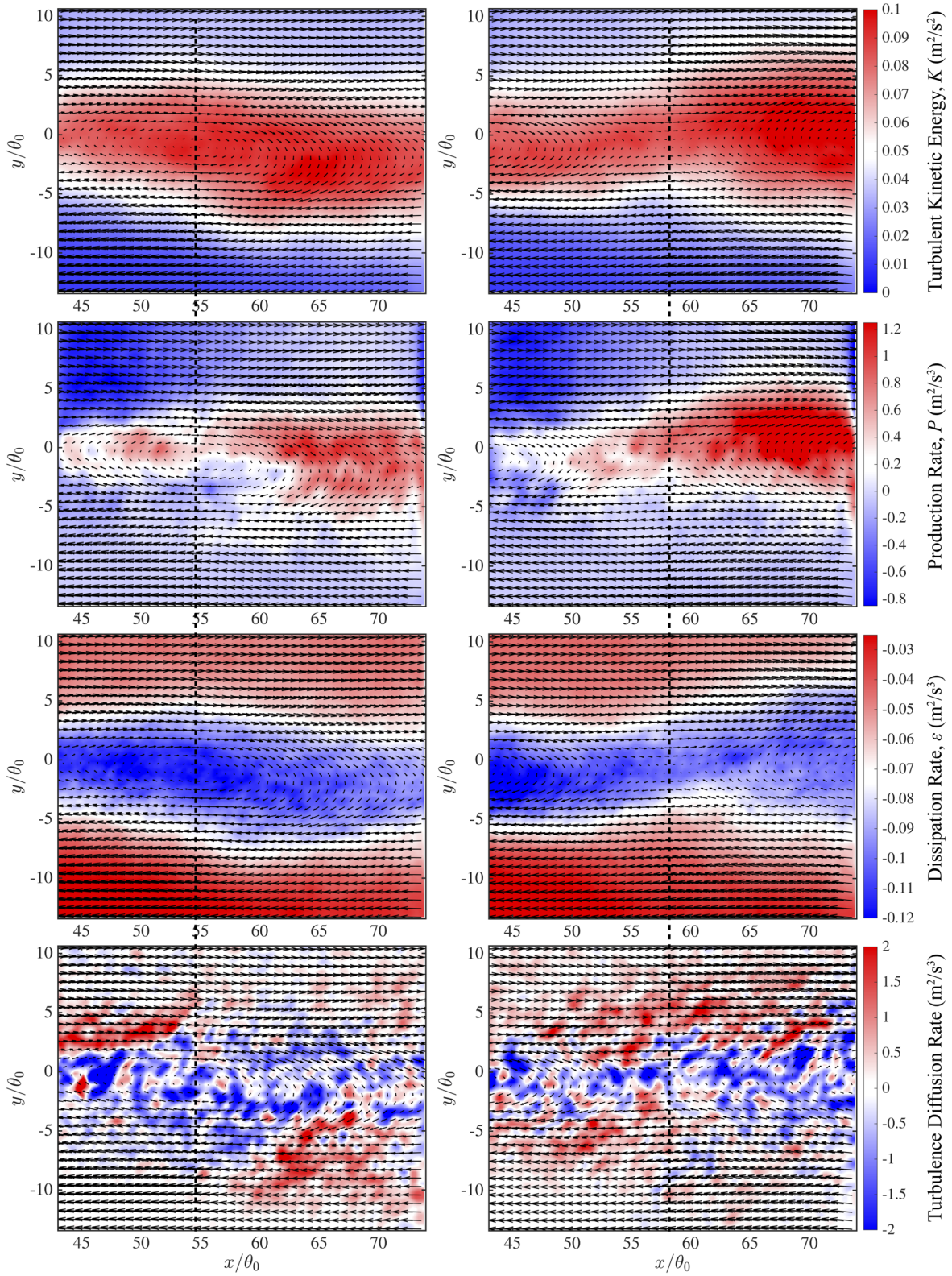


**Fig. 13** Phase-averaged maps (from *top to bottom*) of total turbulent kinetic energy ($K$), production rate ($P$), dissipation rate ($\varepsilon$), and turbulence diffusion rate ($TD$) for two phase-average instances overlaid with Galilean-transformed 2D-vector field to emphasize the spanwise vortical region (*left column*), and the braid (*right column*) region between the vortices. Dashed vertical black lines (– –) shown here pass through the vortical core and braid (saddle point) in the left and right columns, respectively

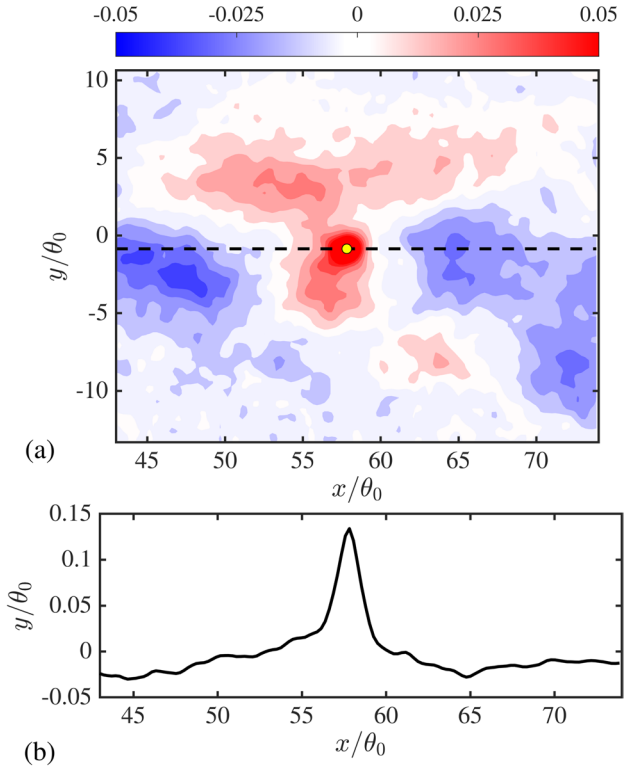


**Fig. 14** **a** Two-point correlation map between production and dissipation rate, $\rho_{P,D}$. The reference point, $(x_0, y_0, z_0)$, shown with a yellow-filled circle is located on the shear layer centerline. **b** Streamwise slice of $\rho_{P,D}$ at $y_0$ along the horizontal dashed black line (– –) shown in (a)

emphasize the rotational coherent motions. The figure shows the spatial distribution of TKE ($K$), production rate ($P$), dissipation rate ($\varepsilon$), and turbulence diffusion rate ($TD$) in the vortical region (left column) and braid region (right column). The TKE contour reveals a relatively higher amount of energy concentrated at the outer edges of the coherent motions (upstream and downstream) than at the vortex core. Moreover, comparatively lower energy is concentrated in the braid region, aligning with the findings of Loucks and Wallace (2012) on TSSL.

The contour maps of the production rate reveal a disparity in turbulence production between the outer edges (downstream and upstream boundaries) of roll-ups, where rolls interact with braids and the vortex cores. These outer edges display significantly higher rates of turbulence production compared to the cores, consistent with the observations of Diorio et al (2007).

Though the dissipation rate field is not as localized as the production field, it exhibits a somehow contrasting behavior, with seemingly greater levels of dissipation rates within the vortex cores as opposed to the braid region. This implies that a substantial portion of the turbulence generated within the shear layer, specifically at the outer edges of the coherent vortices, is dissipated at higher rates within the core of the vortices—a region with larger density of dissipative flow scales. These observations indicate distinct spatial separation between locations of maximum production and dissipation rates within the coherent motions, a pattern that becomes apparent in the two-point correlation map of production and dissipation, $\rho_{P,D}$ shown in Fig. 14.

$$\rho_{P,D} = \frac{\overline{P'(x,y,z,t)D'(x_0,y_0,z_0,t)}}{\sqrt{\overline{P'(x,y,z,t)^2}}\sqrt{\overline{D'(x_0,y_0,z_0,t)^2}}} \tag{6}$$

where $P'$ and $D'$ are fluctuating components of production and dissipation rates, respectively. The map shown here is spanwise-averaged on account of homogeneity in this direction. The map reveals alternating negative and positive correlations between the two turbulence quantities, providing evidence for the presence of alternating coherent motions as well as the spatial distribution of production and dissipation sites in the flow. A streamwise slice along the dashed line (shown in Fig. 14a) of the 3D correlation field $\rho_{P,D}$ is presented in Fig. 14b. The plot shows the alternating correlation behavior between the two quantities. Furthermore, the streamwise spatial separation between the positive correlation peak and negative minima closely matches the streamwise separation between the vortical core and its outer edges, or half the separation between the vortex core and saddle point. This observation reinforces the claim that a distinct spatial separation exists between the peak production and dissipation sites within the mixing layer.

Refer to the contour maps corresponding to the turbulence diffusion rate in Fig. 13, the vortical region shows larger concentration of negative values for turbulence diffusion rates indicating higher degree of mixing, consistent with the larger dissipation rates concentration in the region. Furthermore, apart from braids exhibiting considerable dissipation rates, they exhibit predominantly negative turbulence diffusion rate that appears to form a channel connecting the two adjacent coherent structures. They seem to serve as conduit for exchanging turbulence generated at the region of the braid and vortex intersection where larger scales are stretched to the vortex cores where it eventually gets dissipated. These results suggest that the intersection of the braid and vortices is a key region for energy production, while the vortex region favors energy dissipation.

Besides, predominantly positive turbulence diffusion rates coincide with regions where $u'$ and $v'$ exhibit the same sign, particularly noticeable at the lower right and upper left region of the outer edge of the vortical region observed in Fig. 13 (left). The same behavior can also be observed in Fig. 13 (right). This behavior reiterates that the kinetic energy is generated at the vortex-braid intersection and is subsequently transported as the vortices rotate clockwise

and develop downstream (see turbulence diffusion term in Eq. 5). This strengthens the proposition that turbulence is generated primarily outside the vortical region and then transported toward the cores where it is dissipated.

## 5 Conclusion

Time-resolved 3D-PTV technique is used to study the evolution of a wall boundary layer into a self-similar single-stream shear layer (SSSL). The experiments are conducted using a custom-designed high Reynolds number ($Re_\tau \approx 1\,240$) water tunnel facility. Particle trajectory data are utilized to obtain a three-dimensional velocity field within the boundary layer, its subsequent separation, and development into a self-similar SSSL. The region of interest ranges from $-23 \lesssim x/\theta_0 \lesssim 73$, where $\theta_0$ is the momentum thickness near the separation edge, allowing for comprehensive visualization and analysis of the developing flow coherent motions within the mixing layer. A hybrid approach combining adaptive ensemble binning (EB) and adaptive Gaussian weighting (AGW) is implemented to interpolate the unstructured velocity data onto a structured grid (i.e., from Lagrangian to Eulerian description) at a relatively lower computational cost than other advanced methods while maintaining competent accuracy.

The analysis of the statistical parameters of the mixing layer reveals that self-similarity is attained at a streamwise distance of $\approx 55\theta_0$ from the separation edge, a distance significantly shorter than previously reported in the literature. On comparison of growth rates parameters, such as shear layer width, momentum, and vorticity thickness with past studies poses interesting questions about a potential "universal" scaling that unifies both single- and two-stream shear layers. Besides, the faster growth rate of the mixing layer width on the high-speed side (relative to the mixing layer centerline) with larger free-stream turbulence intensity compared to the zero-speed side provides further evidence for the "nibbling" mechanism to be the primary driving entrainment mechanism in mixing layers.

The separation of BL or sudden flow expansion at the separation edge leads to a high streamwise velocity gradient downstream, $\frac{\partial \overline{U}}{\partial x}$, resulting in a negative turbulence production immediately downstream to the separation edge. With the production term acting as an energy sink, the viscous diffusion term, which otherwise remains negligible, increases in magnitude, leading to a viscous-dominated region reflected in the region's flow morphology which is later confirmed upon TKE budget analysis in the region.

Utilizing the instantaneous maps in self-similar region, phase-averaged maps are obtained to find that the intersection region between outer edges of vortices and braids display high production rates. On the other hand, vortex cores favor turbulence dissipation. A two-point correlation between production and dissipation rates confirms the presence of spatial separation between peak production and dissipation regions. Additionally, the phase-averaged turbulence diffusion rate maps reveal a higher degree of homogeneous distribution or mixing within the vortex region, in contrast to the braid region. Notably, the braid region appears to act as a conduit, effectively facilitating the diffusion of turbulence generated at the intersection of the braid and vortex between adjacent spanwise vortices.

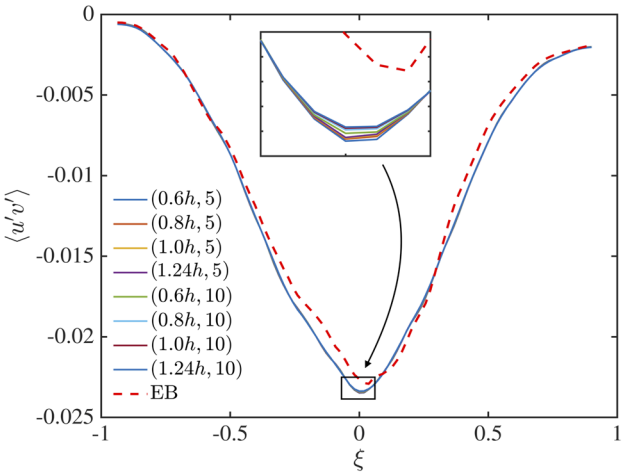


**Fig. 15** Comparison of mean Reynolds shear stress profiles at a location within Zone3 for different combination of Gaussian rms width, $H$ (= $0.6h, 0.8h, 1.0h$, and $1.24h$where his grid spacing), and nearest number of particles to a grid position, $n_p$ (= 5, 10) utilized for interpolation. Profile obtained using ensemble binning (— —) is included for comparison

## Appendix I

### Influence of interpolation parameters

The accuracy and spatial filtering of the data interpolated over structured grids using AGW depend on several factors, including the rms width of the Gaussian weighting function, grid spacing, and particle density over a chosen grid spacing. This section presents a test evaluating the impact of these parameters with the hybrid approach adopted in the present work that combines the technique detailed in Tirelli et al (2023) and AGW (Agüí and Jimenez 1987). Figure 15 showcases mean Reynolds shear stress profiles within the self-similar region for various Gaussian rms width values ($H = 0.6h, 0.8h, 1.0h$, and $1.24h$) and the nearest PTV

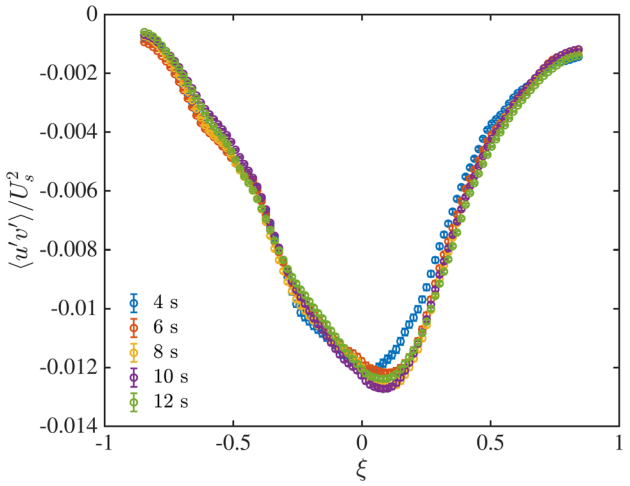


**Fig. 16** Mean Reynolds shear stress profiles within Zone3 for data realizations ranging from 4 s (16,000 realizations) to 12 s (48,000 realizations) with 2 s increments

particles to the grid location ($n_{p=5}$, 10) employed for interpolation. Remarkably, the profiles exhibit minimal variation among the considered cases, highlighting the marginal filtering effect of the interpolation method when using velocity fluctuation data for interpolation rather than instantaneous velocity data. Additionally, with the hybrid approach, AGW offers significant advantage over computationally taxing data regularization techniques by providing accurate and significantly less filtered instantaneous maps for higher-order parameters such as Reynolds stresses.

### Data convergence test

A convergence test is performed to determine if the number of instantaneous realizations captured in the present study is enough to estimate statistical descriptors accurately. To this end, 48,000 instantaneous realizations of three-4 s long data sets (for Zone3) are divided into 5 subsets with an increasing number of realizations (or capture time) equivalent to 8000 realizations (or 2 s capture time).

Figure 16 shows the mean Reynolds shear stress profile at a location within Zone3 for the different subsets. The Reynolds shear stress profile is chosen to assess statistical convergence as it is sensitive to streamwise and cross-stream fluctuations. The profiles nearly collapse over each other for the data realization lengths $\geq$ 6 s, suggesting that the data set must be collected over at least 6 s to ensure convergence of statistical descriptors within Zone3. On the other hand, data realization lengths of 1 s and 2 s are deemed sufficient for the statistical descriptors in Zone1 and Zone2, respectively (not shown here).

Though the spanwise thickness of the ROI is relatively small (approximately 1/8 of the width and 1/5 of the height of the ROI), the data are also tested for spanwise variability to ensure the validity of spanwise averaging. For instance, the results for the Reynolds stress shown in Fig. 16 are observed to deviate no more than $\pm 1\%$ of their respective average values. This result gives confidence that flow heterogeneity in the spanwise direction is not significant enough to affect spanwise averaging.

## Appendix II

### Uncertainty analysis

The uncertainties associated with mean statistical quantities, as outlined in Sciacchitano and Wieneke (2016), are given by,

$$\Delta_{\overline{u}} = \frac{\sigma_u}{\sqrt{N}} \tag{7}$$

$$\sigma_u \approx \sqrt{\sigma_{u,f}^2 + \overline{\Delta_u^2}} \tag{8}$$

$$\Delta_{\overline{u_i' u_i'}} \approx \overline{u_i' u_i'} \sqrt{\frac{2}{N}} \tag{9}$$

$$\Delta_{\overline{u'v'}} = \sigma_u \sigma_v \sqrt{\frac{1+\rho_{uv}^2}{N-1}} \tag{10}$$

$$\Delta_K = \sqrt{\left(\overline{u'^2}\right)^2 + \left(\overline{v'^2}\right)^2 + \left(\overline{w'^2}\right)^2} \cdot \sqrt{\frac{1}{2N}} \tag{11}$$

where $N$ is the total number of realizations, $\sigma_{u,f}$ represents the standard deviation of true velocity fluctuations at a grid point, and $\overline{\Delta_u^2}$ is the average square of the uncertainty in instantaneous velocity, denoted by $\Delta_u$. This uncertainty is linked to interpolation errors across the grids of the instantaneous velocity $u_h$. $\Delta_{\overline{u_i' u_i'}}$ and $\Delta_{\overline{u'v'}}$ are uncertainty for Reynolds normal stresses and shear stresses, respectively; $\rho_{uv}$ is cross-correlation coefficient between $u$ and $v$. Error bars for the higher-order turbulence parameters reported in the present work are similarly estimated.

**Acknowledgements** Present work is performed under the auspices of the U.S. Department of Energy (DOE). Financial support comes from Los Alamos National Laboratory (LANL), Office of Experimental Sciences (OES). LANL, an affirmative action/equal opportunity employer, is managed by Triad National Security, LLC, for the National Nuclear Security Administration of the DOE under contract 89233218CNA000001. High-performance computing resources are provided by ICER at Michigan State University.

**Author contributions** R.M-A. and D.L. designed the experiments. A.K.G. conducted the experiments, processed the data and wrote the main manuscript. R.M-A. and A.K.G. analyzed the results. D.L. critiqued the analysis and suggested changes. All authors reviewed and edited the manuscript.

**Funding** This study was funded by Los Alamos National Laboratory under Subaward No. 527464.

**Data availability** The authors can provide copies of the raw data gathered in this study upon request.

## Declarations

**Conflict of interest** The authors do not have any financial or personal interests regarding the results of this work.



## References

Agüera N, Cafiero G, Astarita T, Discetti S (2016) Ensemble 3D PTV for high resolution turbulent statistics. Meas Sci Technol 27(12):124011

Agüí JC, Jimenez J (1987) On the performance of particle tracking. J Fluid Mech 185:447–468

Attili A, Bisetti F (2012) Statistics and scaling of turbulence in a spatially developing mixing layer at $Re_\lambda = 250$. Phys Fluids 24(3):035109

Balamurugan G, Rodda A, Philip J, Mandal A (2020) Characteristics of the turbulent non-turbulent interface in a spatially evolving turbulent mixing layer. J Fluid Mech 894:A4

Balaras E, Piomelli U, Wallace JM (2001) Self-similar states in turbulent mixing layers. J Fluid Mech 446:1–24

Baltzer JR, Livescu D (2020) Variable-density effects in incompressible non-buoyant shear-driven turbulent mixing layers. J Fluid Mech 900:A16

Bell JH, Mehta RD (1990) Development of a two-stream mixing layer from tripped and untripped boundary layers. AIAA J 28(12):2034–2042

Browand F, Latigo B (1979) Growth of the two-dimensional mixing layer from a turbulent and nonturbulent boundary layer. Phys Fluids 22(6):1011–1019

Browand F, Troutt T (1985) The turbulent mixing layer: geometry of large vortices. J Fluid Mech 158:489–509

Brown GL, Roshko A (1974) On density effects and large structure in turbulent mixing layers. J Fluid Mech 64(4):775–816

Campbell I, Turner J (1985) Turbulent mixing between fluids with different viscosities. Nature 313(5997):39–42

Casa L, Krueger P (2013) Radial basis function interpolation of unstructured, three-dimensional, volumetric particle tracking velocimetry data. Meas Sci Technol 24(6):065304

Champagne F, Pao Y, Wygnanski IJ (1976) On the two-dimensional mixing region. J Fluid Mech 74(2):209–250

Chong MS, Perry AE, Cantwell BJ (1990) A general classification of three-dimensional flow fields. Phys Fluids A 2(5):765–777

Cimarelli A, Leonforte A, De Angelis E, Crivellini A, Angeli D (2019) On negative turbulence production phenomena in the shear layer of separating and reattaching flows. Phys Lett A 383(10):1019–1026

Clauser FH (1954) Turbulent boundary layers in adverse pressure gradients. J Aeronaut Sci 21(2):91–108

Clauser FH (1956) The turbulent boundary layer. Adv Appl Mech 4:1–51

Dimotakis P (1991) Turbulent free shear layer mixing and combustion. High Speed Flight Propuls Syst 137:265–340

Diorio J, Kelley DH, Wallace JM (2007) The spatial relationships between dissipation and production rates and vortical structures in turbulent boundary and mixing layers. Phys Fluids 19(3):035101

Dixit SA, Ramesh O (2009) Determination of skin friction in strong pressure-gradient equilibrium and near-equilibrium turbulent boundary layers. Exp Fluids 47(6):1045–1058

D'Ovidio A, Coats C (2013) Organized large structure in the post-transition mixing layer. Part 1. Experimental evidence. J Fluid Mech 737:466–498

Gesemann S (2015) From particle tracks to velocity and acceleration fields using B-splines and penalties. arXiv preprint arXiv:1510.09034

Grinstein F, Oran E, Boris J (1986) Numerical simulations of asymmetric mixing in planar shear flows. J Fluid Mech 165:201–220

Harang A, Thual O, Brancher P, Bonometti T (2014) Kelvin-Helmholtz instability in the presence of variable viscosity for mudflow resuspension in estuaries. Environ Fluid Mech 14(4):743–769

Hussain A, Zaman K (1985) An experimental study of organized motions in the turbulent plane mixing layer. J Fluid Mech 159:85–104

Hussain A, Zedan M (1978) Effects of the initial condition on the axisymmetric free shear layer: effect of the initial fluctuation level. Phys Fluids 21(9):1475–1481

Hussain A, Zedan M (1978) Effects of the initial condition on the axisymmetric free shear layer: effects of the initial momentum thickness. Phys Fluids 21(7):1100–1112

Jeon YJ, Müller M, Michaelis D (2022) Fine scale reconstruction (VIC#) by implementing additional constraints and coarse-grid approximation into VIC+. Exp Fluids 63(4):1–24

Jiménez J, Hoyas S, Simens MP, Mizuno Y (2010) Turbulent boundary layers and channels at moderate Reynolds numbers. J Fluid Mech 657:335–360

Kailas S, Narasimha R (1999) The eduction of structures from flow imagery using wavelets part I. Mixing layer. Exp Fluids 27(2):167–174

Keller J, Ellzey J, Pitz R, Shepherd I, Daily J (1988) The structure and dynamics of reacting plane mixing layers. Exp Fluids 6(1):33–43

Koochesfahani M, Dimotakis P, Broadwell J (1983) Chemically reacting turbulent shear layers technical report. California Institute of Technology, Pasadena

Lasheras J, Cho J, Maxworthy T (1986) On the origin and evolution of streamwise vortical structures in a plane, free shear layer. J Fluid Mech 172:231–258

Lee H, Park HJ, Kim M, Han J, Hwang W (2022) The effect of perspective error on 2d PIV measurements of homogeneous isotropic turbulence. Exp Fluids 63(8):122

Liepmann HW, Laufer J (1947) Investigations of free turbulent mixing. Technical Reports. National advisory committee for aeronautics technical note No. 1257, NASA

Liu X, Thomas FO (2004) Measurement of the turbulent kinetic energy budget of a planar wake flow in pressure gradients. Exp Fluids 37(4):469–482

London AL, Klopfer G, Wolf S (1968) Oblique flow headers for heat exchangers. J Eng Gas Turbines Power 90:284–285

Loucks RB, Wallace JM (2012) Velocity and velocity gradient based properties of a turbulent plane mixing layer. J Fluid Mech 699:280–319

Mathew J, Basu AJ (2002) Some characteristics of entrainment at a cylindrical turbulence boundary. Phys Fluids 14(7):2065–2072

McMullan WA, Garrett SJ (2016) Initial condition effects on large scale structure in numerical simulations of plane mixing layers. Phys Fluids 28(1):015111

McMullan WA, Gao S, Coats CM (2015) Organised large structure in the post-transition mixing layer. Part 2. Large-eddy simulation. J Fluid Mech 762:302–343

Mehta R, Westphal R (1986) Near-field turbulence properties of single- and two-stream plane mixing layers. Exp Fluids 4(5):257–266

Mejia-Alvarez R (2010) Experimental study of low-order models of highly-irregular roughness and their impact on turbulent boundary layers. PhD thesis, University of Illinois at Urbana-Champaign

Mills R (1968) Numerical and experimental investigations of the shear layer between two parallel streams. J Fluid Mech 33(3):591–616

Morris SC, Foss JF (2003) Turbulent boundary layer to single-stream shear layer: the transition region. J Fluid Mech 494:187–221

Novara M, Ianiro A, Scarano F (2012) Adaptive interrogation for 3D-PIV. Meas Sci Technol 24(2):024012

Patel RP (1973) An experimental study of a plane mixing layer. AIAA J 11(1):67–71

Pedocchi F, Martin JE, García MH (2008) Inexpensive fluorescent particles for large-scale experiments using particle image velocimetry. Exp Fluids 45(1):183–186

Perry A, Li JD (1990) Experimental support for the attached-eddy hypothesis in zero-pressure-gradient turbulent boundary layers. J Fluid Mech 218:405–438

Pope SB (2000) Turbulent flows. Cambridge University Press, Cambridge

Raiola M, Lopez-Nuñez E, Cafiero G, Discetti S (2020) Adaptive ensemble PTV. Meas Sci Technol 31(8):085301

Rajagopalan S, Ko N (1996) Velocity and spanwise vorticity measurements in an excited mixing layer of a plane jet. Exp Fluids 20(5):346–357

Rogers MM, Moser RD (1994) Direct simulation of a self-similar turbulent mixing layer. Phys Fluids 6(2):903–923

Schanz D, Gesemann S, Schröder A (2016) Shake-The-Box: Lagrangian particle tracking at high particle image densities. Exp Fluids 57(5):70

Schlichting H, Gersten K (2000) Fundamentals of boundary-layer theory. Springer, Berlin, pp 29–49

Schneiders JF, Scarano F (2016) Dense velocity reconstruction from tomographic PTV with material derivatives. Exp Fluids 57(9):1–22

Schultz M, Flack K (2007) The rough-wall turbulent boundary layer from the hydraulically smooth to the fully rough regime. J Fluid Mech 580:381–405

Sciacchitano A, Wieneke B (2016) PIV uncertainty propagation. Meas Sci Technol 27(8):084006

Sharan N, Matheou G, Dimotakis PE (2019) Turbulent shear-layer mixing: initial conditions, and direct-numerical and large-eddy simulations. J Fluid Mech 877:35–81

Suryanarayanan S, Narasimha R (2017) Insights into the growth rate of spatially evolving plane turbulent free-shear layers from 2d vortex-gas simulations. Phys Fluids 29(2):020708

Talbot B, Danaila L, Renou B (2013) Variable-viscosity mixing in the very near field of a round jet. Phys Scr T 155:014006

Taveira RR, Diogo JS, Lopes DC, da Silva CB (2013) Lagrangian statistics across the turbulent-nonturbulent interface in a turbulent plane jet. Phys Rev E 88(4):043001

Tirelli I, Ianiro A, Discetti S (2023) A simple trick to improve the accuracy of PIV/PTV data. Exp Therm Fluid Sci 145:110872

Weber CR, Clark DS, Cook AW, Busby LE, Robey HF (2014) Inhibition of turbulence in inertial confinement fusion hot spots by viscous dissipation. Phys Rev E 89:053106

Wei T, Li Z, Livescu D (2022) Scaling patch analysis of planar turbulent mixing layers. Phys Fluids 34(11):115120

Wetzel J, Arndt R (1994) Hydrodynamic design considerations for hydroacoustic facilities: part I-flow quality. ASME J Fluids Eng 116(2):324–331

Wieneke B (2008) Volume self-calibration for 3D particle image velocimetry. Exp Fluids 45(4):549–556

Wieneke B (2012) Iterative reconstruction of volumetric particle distribution. Meas Sci Technol 24(2):024008

Wiener N (1949) Extrapolation, interpolation, and smoothing of stationary time series: with engineering applications, vol 2. MIT press Cambridge, MA

Wygnanski I, Fiedler HE (1970) The two-dimensional mixing region. J Fluid Mech 41(2):327–361